

## Appendix B:

# Remote Sensing Imagery and Principles: Foundations and Applications for Battlefield Damage Assessment of Urban Structures



*Figure 1: Sentinel-2 Satellite, Source: ESA*

Author : Marco Heinzen

## Contents

Appendix B: .....	1
1. Introduction to Remote Sensing .....	3
2. Active and Passive Sensors .....	6
3. Passive Sensors .....	8
3.1. Optical .....	9
3.2. Fundamental Analysis Methods .....	13
3.3. Principles of Spectral Indices .....	14
3.4. Spectral Similarity and Unmixing Approaches .....	15
4. Active Sensors .....	18
4.1. Basic Principles of Radar .....	19
4.2. Sidelooking Radar .....	21
4.3. Synthetic Aperture Radar (SAR) .....	22
4.4. Advanced SAR Techniques: InSAR .....	34
5. Glossary and Definitions .....	36
6. Acronyms and Abbreviations .....	38
7. List of Figures .....	40
8. List of Tables .....	41
9. References .....	42
10. Disclaimer .....	50

## 1. Introduction to Remote Sensing

Remote sensing is the science of acquiring information about the Earth's surface and atmosphere without direct contact, typically by means of satellites, aircraft, or drones. The fundamental principle lies in detecting electromagnetic radiation that is either naturally emitted or reflected by objects or artificially transmitted by a sensor and then scattered back. Since the launch of Landsat-1 in 1972, Earth observation has developed into a multidisciplinary field that integrates optical, thermal, radar, and hyperspectral imaging (James B. Campbell & Randolph H. Wynne, 2011; Richards, 2022).

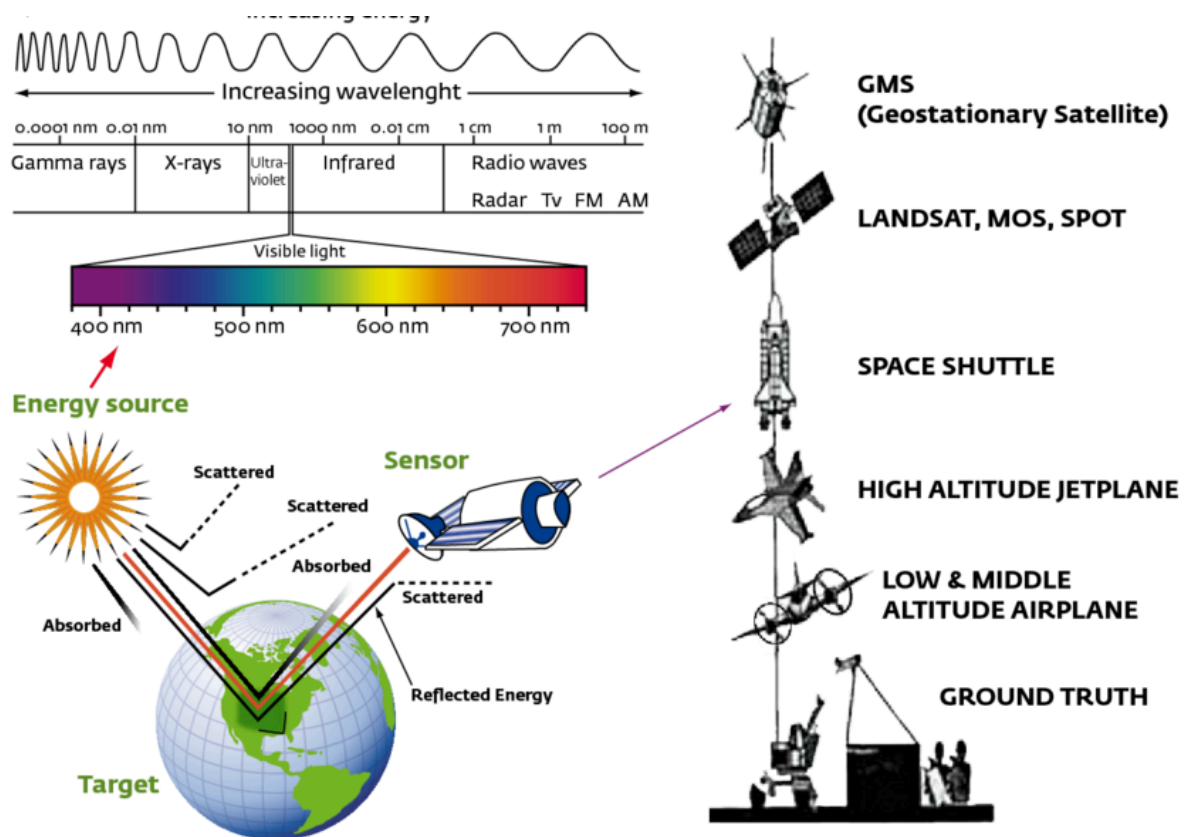


Figure 2: Theory of remote sensing of the earth Electromagnetic spectrum of energy radiations Remote sensing platforms with Sensors on board (Omuto et al., 2012)



Figure 3: DJI Matrice 300 RTK Drone equipped with Zenmuse P1 camera during the mission at Fuglebekken catchment. (Alphonse et al., 2023)

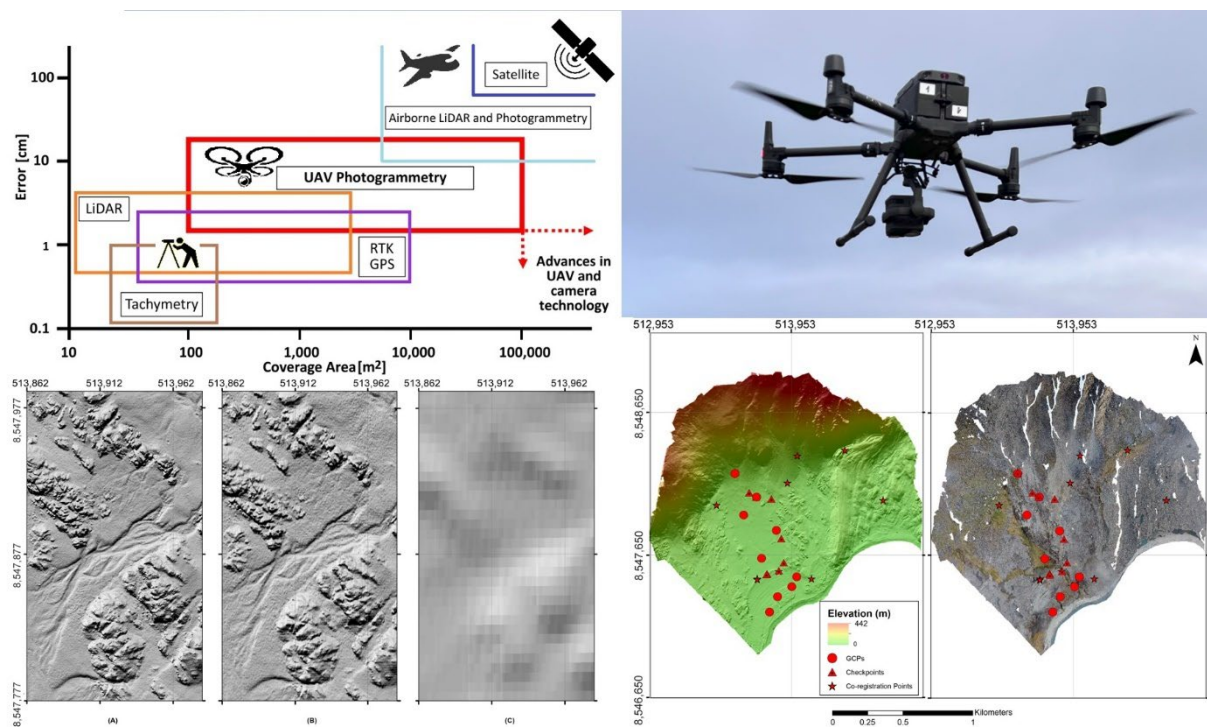


Figure 4: Graphical Abstract (Alphonse et al., 2023)



The translation from the real world into a remote sensing image is mediated by what is known as the sensor transfer function, a conceptual model describing how the attributes of the observation system -spectral range, spatial resolution, temporal repeat, and atmospheric sensitivity - determine which characteristics of the real world are captured and which are ignored (Richards, 2022). The process is inherently selective and lossy, meaning that only specific features of the observed scene are preserved in the data, while others are lost.

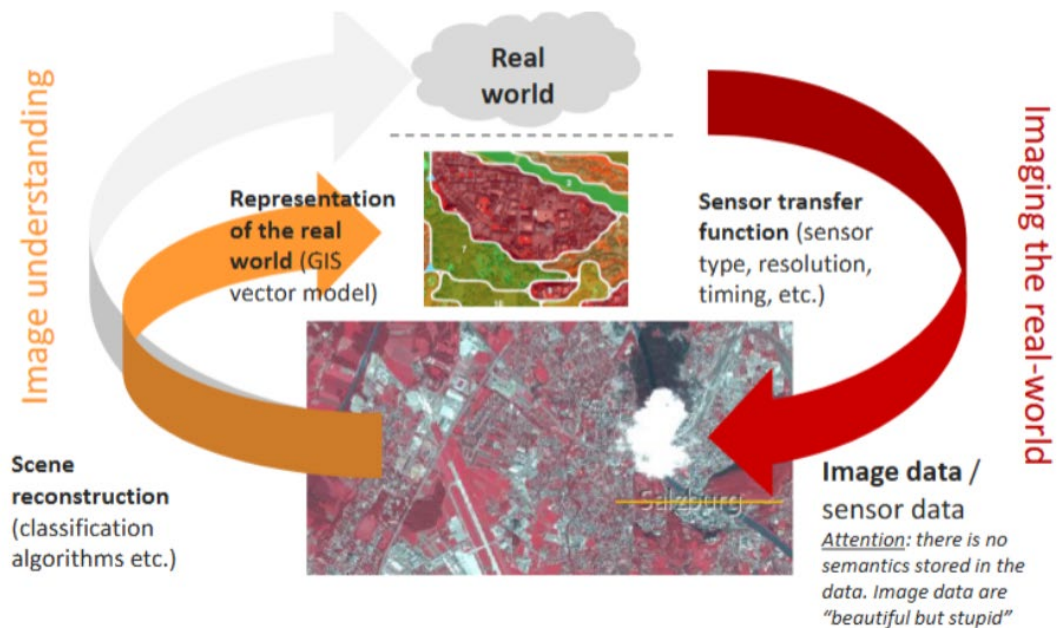


Figure 5: From the real world to an image of it, to scene reconstruction. Image from UNIGIS Salzburg based on (Blaschke, 2010)

The reconstruction of meaningful information from such images requires interpretation, a process known as scene reconstruction. Scene reconstruction combines sensor data with contextual information and prior knowledge, ultimately transforming pixels into semantic representations such as land cover classes or object categories (Blaschke, 2010). Improvements in remote sensing can be achieved either by enhancing the quantity of the data (for example, hyperspectral rather than multispectral imagery), by refining methods of analysis such as moving from pixel-based to object-based approaches, or by enriching interpretation with external knowledge such as classifiers and contextual models (Blaschke, 2010; Richards, 2022). Figure 5 illustrates this process of transformation from the real world to an image and then to scene reconstruction, showing how raw sensor data without inherent meaning can be turned into a representation of the environment through interpretation.

## 2. Active and Passive Sensors

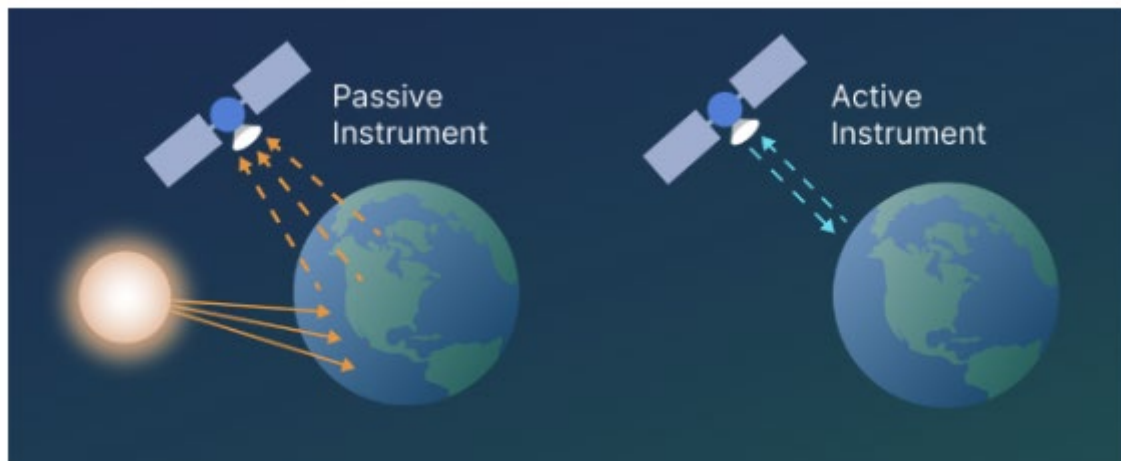


Figure 6: Active and Passive Sensors. Source: NASA

Remote sensing sensors can be broadly divided into passive and active systems. Passive sensors rely on natural sources of energy, most commonly the sun, to measure reflected radiation in the visible to shortwave infrared part of the spectrum or emitted longwave infrared radiation in the thermal domain (James B. Campbell & Randolph H. Wynne, 2011; Jensen, 2016). Active sensors, in contrast, generate their own signal, usually in the form of microwave or laser pulses, transmit it towards the Earth's surface, and measure the backscattered return (Woodhouse, 2017). This fundamental distinction determines their suitability for different applications. Passive instruments such as Landsat and Sentinel-2 are restricted to daytime acquisitions and require cloud-free conditions, which limits their usability in persistently cloudy regions (Berger et al., 2012; Wulder et al., 2019). Active instruments such as Synthetic Aperture Radar operate independently of sunlight and can penetrate clouds, haze, and even vegetation canopies, making them invaluable for all-weather, day-and-night monitoring (Meyer, 2019; Moreira et al., 2013). The choice of a sensor type is closely tied to the observation target and the environmental conditions during acquisition.

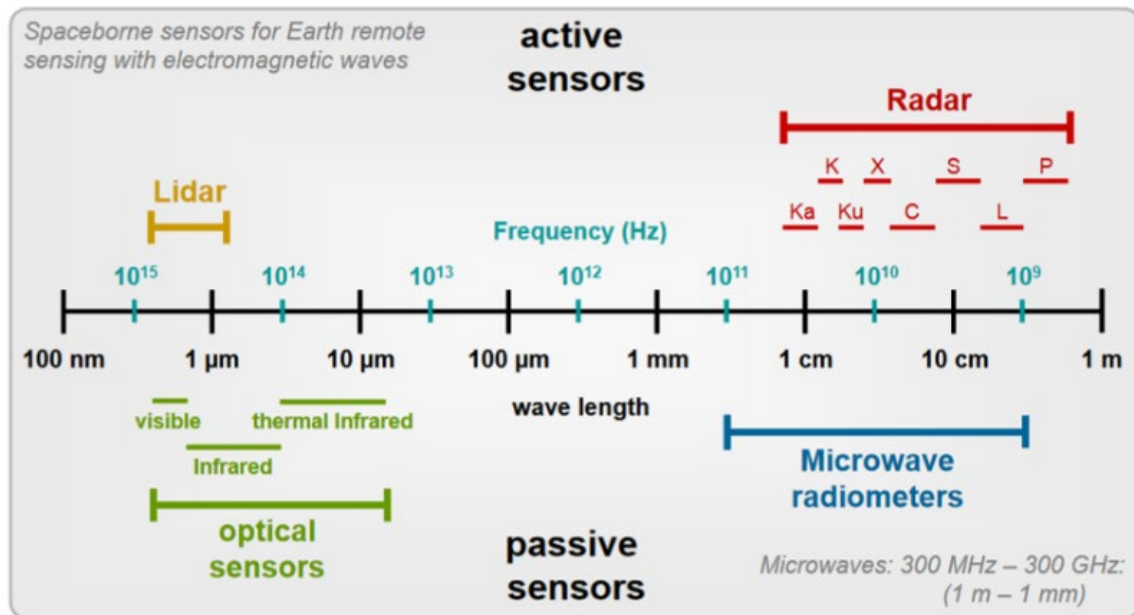


Figure 7: The electromagnetic spectrum typically used in remote sensing, and spectral reflectance curves show the distinct signatures of vegetation, soil, and water, which are fundamental for interpretation (Jensen, 2016).

Multispectral systems such as Landsat and Sentinel-2 have long been the backbone of vegetation monitoring, while hyperspectral instruments provide detailed discrimination of plant physiological traits and land cover classes (Berger et al., 2012; Wulder et al., 2019). Synthetic Aperture Radar, by contrast, is largely unaffected by clouds or solar illumination and is therefore indispensable for all-weather, day-and-night monitoring, particularly in persistently cloudy regions or when structural and moisture-related information is required (Meyer, 2019; Moreira et al., 2013).

### 3. Passive Sensors

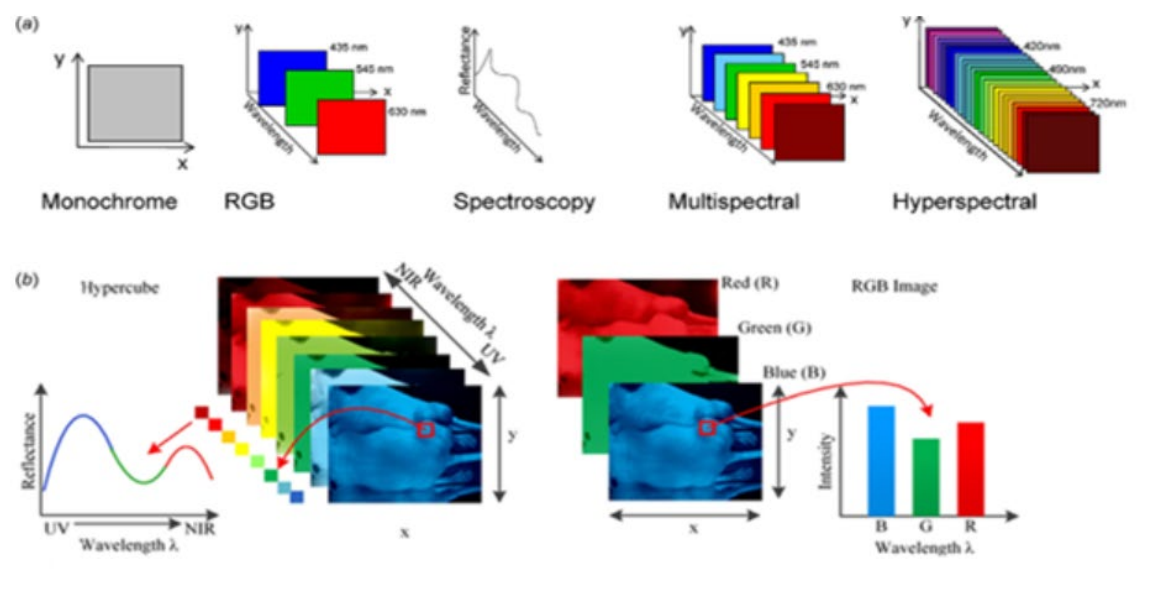


Figure 8: Monochrome, multispectral and hyperspectral imaging visualized (Mehta et al., 2018)

Passive instruments include both optical and thermal sensors. Optical systems measure reflected solar energy in the visible, near-infrared, and shortwave infrared regions, while thermal systems measure emitted longwave radiation that corresponds to surface temperature (Jensen, 2016). Each type of land cover exhibits a characteristic spectral response that can be used for identification: vegetation shows strong absorption in the red wavelengths due to chlorophyll and high reflectance in the near-infrared owing to leaf structure, soils exhibit wavelength-dependent reflectance curves determined by their mineral and organic composition, and water bodies display strong absorption in the near-infrared and shortwave infrared, making them appear dark in these bands (James B. Campbell & Randolph H. Wynne, 2011; Richards, 2022). These characteristic signatures form the basis of optical remote sensing analysis. However, passive systems are sensitive to atmospheric interference. Clouds, aerosols, and water vapor can significantly reduce data quality and complicate interpretation (Richards, 2022). Despite this limitation, passive sensors have been the backbone of Earth observation because of their long temporal continuity and global coverage. The Landsat program, operating since 1972, provides the longest continuous record of multispectral Earth observation (Wulder et al., 2019). Instruments such as MODIS, launched in 1999, provide daily global coverage across 36 spectral bands (Justice et al., 1998). Sentinel-2, launched in 2015, has further enhanced these capabilities with higher spatial resolution and additional red-edge bands specifically useful for vegetation analysis (Berger et al., 2012). Multispectral and hyperspectral satellite instruments are passive sensors, relying on reflected solar energy (James B. Campbell & Randolph H. Wynne, 2011; Jensen, 2016).



### 3.1. Optical



Figure 9: Sentinel 2 - Optical Image / True Colour Composite. Source: ESA

Optical remote sensing is the most widely used passive modality. Its systems are commonly divided into panchromatic, multispectral, and hyperspectral sensors according to the number and width of spectral bands (James B. Campbell & Randolph H. Wynne, 2011; Jensen, 2016). Panchromatic sensors collect a single broad band of wavelengths, yielding very high spatial resolution but minimal spectral discrimination (Richards, 2022). Multispectral sensors collect data in several broad bands, usually between four and thirteen, which allows differentiation of major land cover classes and has proven effective for agricultural, urban, and environmental monitoring (Drusch et al., 2012; Wulder et al., 2019). Hyperspectral sensors extend this principle by measuring hundreds of narrow, contiguous bands, thereby capturing fine spectral details that allow identification of specific materials and precise quantification of biophysical parameters (Berger et al., 2012; Goetz et al., 1985). Figure 2 illustrates the conceptual distinction between monochrome, multispectral, and hyperspectral imaging (Mehta et al., 2018).

Processing optical data involves several correction steps. Radiometric calibration ensures that measured digital numbers are converted into physical radiance values (Jensen, 2016). Atmospheric correction removes distortions caused by scattering and absorption of gases such as oxygen, ozone, and water vapor. Without such correction, absorption features may be misinterpreted as intrinsic surface properties (Richards, 2022). Geometric correction aligns imagery with the Earth's surface, enabling temporal comparisons and multi-sensor integration. The analysis of optical data is often facilitated through vegetation and water indices. The most widely used of these is the Normalized Difference Vegetation Index (NDVI), which exploits the difference between red and near-infrared reflectance to quantify vegetation greenness (Tucker, 1979). Other indices such as the Normalized Difference Water Index (NDWI) enhance the detection of water bodies (Gao, 1996), while burn indices such as the Normalized Burn Ratio (NBR) provide information on fire damage (Key & Benson, 2006).



Sentinel-2 has extended the capability of such indices by including dedicated red-edge bands, which improve sensitivity to canopy structure and vegetation stress (Drusch et al., 2012). Despite limitations in cloudy regions, optical imagery remains the cornerstone of remote sensing, due to its interpretability, historical continuity, and wide range of applications (James B. Campbell & Randolph H. Wynne, 2011; Wulder et al., 2019).

### 3.1.1. Multispectral Remote Sensing



Figure 10: False colour composite with RGB and NIR, Source: ESA Sentinel-2

Multispectral sensors measure reflected radiation in a limited number of discrete, relatively broad spectral bands. They represent the most widely used passive imaging systems and have formed the backbone of global monitoring for over five decades. The Landsat program, beginning in 1972, is the longest continuous source of multispectral satellite imagery, offering 30 m resolution data in visible, near-infrared, and shortwave infrared bands. Instruments such as the Thematic Mapper (TM), Enhanced Thematic Mapper Plus (ETM+), and Operational Land Imager (OLI) have provided continuity, ensuring consistency across generations of sensors (Wulder et al., 2019).

More recently, the Sentinel-2 MultiSpectral Instrument (MSI) has extended the capability of multispectral observation. With 13 spectral bands at 10-60 m resolution and a five-day revisit cycle, Sentinel-2 provides detailed coverage for agriculture, forestry, and disaster monitoring. Its inclusion of three red-edge bands, specifically designed for vegetation studies, enhances sensitivity to canopy structure and stress (Drusch et al., 2012). Other instruments, such as MODIS on NASA's Terra and Aqua satellites, provide coarser-resolution multispectral data but with daily global coverage and a wide spectral range (Justice et al., 1998).

The limitations of multispectral systems lie in their restricted number of bands, which reduces the ability to discriminate materials with subtle spectral differences. Despite this, their balance

between spatial, temporal, and spectral resolution has made them indispensable for global monitoring. Their relatively low data volume compared to hyperspectral systems allows for efficient processing and long-term archiving. Multispectral data underpin vegetation and water indices, burned area mapping, land cover classification, and agricultural yield estimation, providing a foundation upon which other, more advanced modalities are built (James B. Campbell & Randolph H. Wynne, 2011).

### 3.1.2. Hyperspectral Remote Sensing

	Satellite based					Airplane - based				UAV-based	
Sensor	Hyperion	PROBA-CHRIS	PRISMA	ENMAP	CRISM	AVIRIS	CASI	AISA	HyMap	Headwall	Hyperspec UHD 185 - Firefly
Spectral range [nm]	357-2576	415-1050	400-2500	420-2450	362-3920	400-2500	380-1050	400-970	440-2500	400-1000	450-950
No. of Spectral bands	220	19 or 63	238	242	544	224	288	244	244	270(Nano) 324(Micro)	138
Spectral Resolution [nm]	10	34 or 17	12	6.5 and 10	6.55	10	<3.5	3.3	3.3	6 (Nano) 2.5 (Micro)	4
Operational Altitude [km]	705	830	615	652	300 (over Mars!)	1-20	1-20	1-20	1-20	<0.15	<0.15
Spatial resolution [m]	30	17-36	30	30	15-200	1-20	1-20	1-20	1-20	0.01-0.5	0.01-0.5
Year	2000 - 2017	2001 - 2024	2019 -	2022 --	2006 - 2022	1987 -	1989 -	1996 -	1997 -	2020	2020

Table 1: Overview of Hyperspectral Sensors. Specifications compiled from : (Babey & Anger, 1993; Barnsley et al., 2004; Cocks et al., 1998; Green et al., 1998; Headwall Photonics - Hyperspectral Imaging Systems & Components, n.d.; Table 1 Spectral Characteristics of the CASI Data, n.d.; Kirrilly Pfitzner, 2004; Loizzo et al., 2018; Miko, n.d.; S. Murchie et al., 2007; S. L. Murchie et al., 2009; Pearlman et al., 2003; van der Meer et al., 2012). For UAV-based platforms: Spatial resolution is a typical GSD range for low-altitude UAV operations with standard optics, and that true instrument specifications are spectral range, number of bands, and spectral sampling (Headwall Photonics - Hyperspectral Imaging Systems & Components, n.d.)

Hyperspectral sensors extend the principle of multispectral imaging by capturing hundreds of narrow, contiguous spectral bands, typically with bandwidths of 5-10 nm. This fine spectral resolution enables the detection of diagnostic absorption features related to pigments, minerals, water content, and organic compounds (Clark et al., 2003; Thenkabail et al., 2011). Imaging spectroscopy was first demonstrated with airborne systems such as AVIRIS and

HyMap (Goetz et al., 1985) and has since been deployed on spaceborne platforms, beginning with Hyperion on NASA's EO-1 satellite (Pearlman et al., 2003) and more recently PRISMA (Loizzo et al., 2018) and EnMAP (Guanter et al., 2015).

Hyperspectral imaging provides an almost continuous spectrum for each pixel, allowing quantitative retrieval of biophysical and geochemical parameters. For vegetation, it enables detection of subtle variations in chlorophyll, carotenoids, and water absorption features, which are essential for assessing plant stress and physiological processes. In geology, hyperspectral data allow discrimination of mineral assemblages through their diagnostic absorption features, while in aquatic systems they provide information on water quality indicators such as chlorophyll-a, suspended sediments, and dissolved organic matter (Clark et al., 2003; van der Meer et al., 2012).

Processing hyperspectral data is challenging due to their high dimensionality, inherent noise, and atmospheric interference. Preprocessing typically includes radiometric calibration, atmospheric correction with models such as MODTRAN or FLAASH, and geometric correction to ensure accurate spatial referencing. Because many hyperspectral bands have low signal-to-noise ratios, noise reduction and dimensionality reduction techniques are essential to retain the most informative features (Jensen, 2016; Richards, 2022).

The potential of hyperspectral Earth observation is expanding rapidly with new satellite missions. Italy's PRISMA mission, launched in 2019, provides 30 m resolution data across 239 spectral bands (Loizzo et al., 2018). Germany's EnMAP mission, launched in 2022, delivers global hyperspectral coverage with 30 m spatial resolution and 242 bands (Guanter et al., 2015). Planned missions such as ESA's CHIME and NASA's Surface Biology and Geology (SBG) mission will further expand global hyperspectral capacity, marking the start of a new era in imaging spectroscopy (Guanter et al., 2015; Thenkabail & Lyon, 2016).

### 3.1.3. Vicarious Calibration and Atmospheric Correction

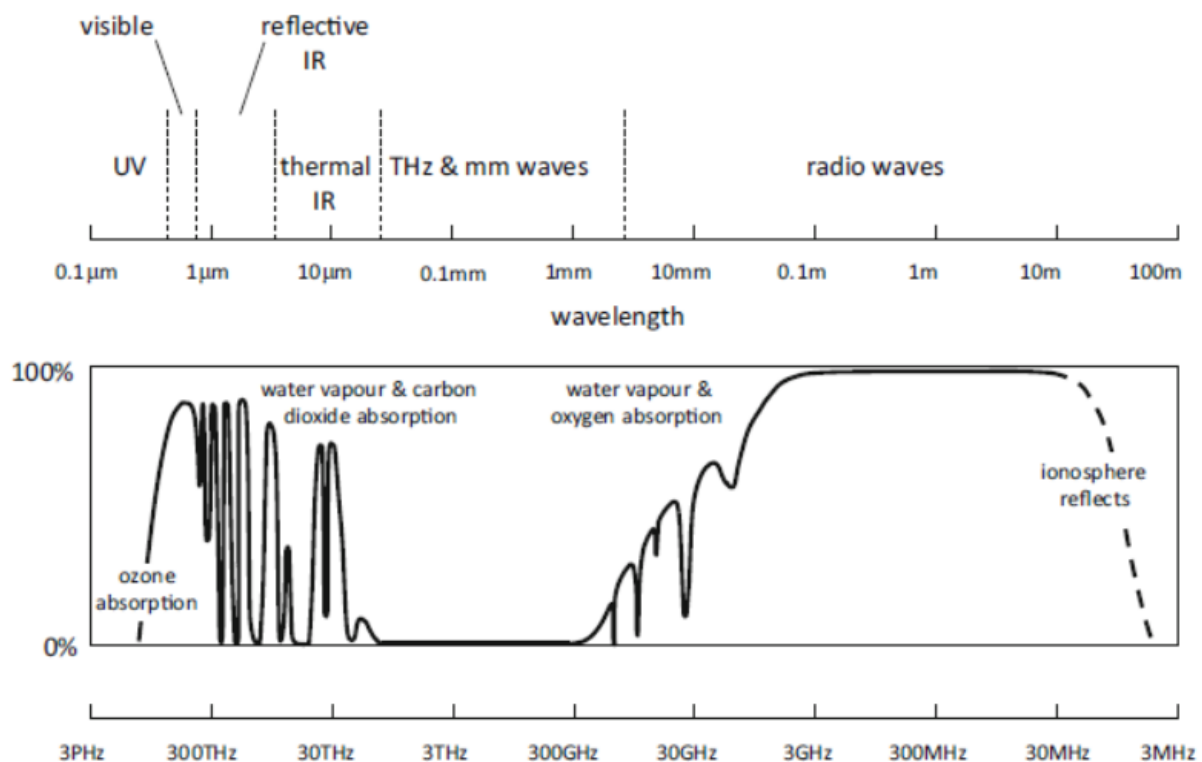


Figure 11: the electromagnetic spectrum and the transmittance through earth's atmosphere (Richards, 2022).

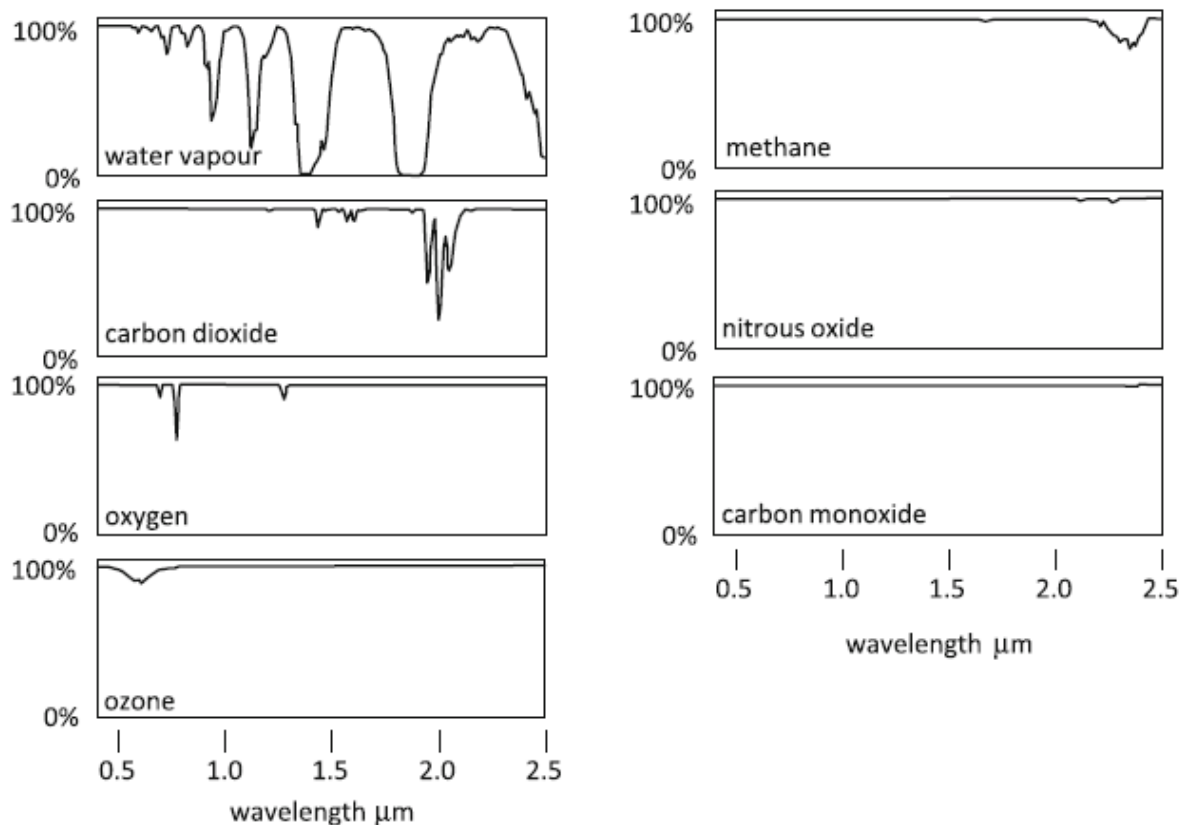


Figure 12: Indicative transmission spectra of the seven most significant atmospheric constituents, the water vapour curve is for a tropical atmosphere (Richards, 2022)

Accurate hyperspectral analysis requires atmospheric correction to convert top-of-atmosphere radiance into bottom-of-atmosphere, or surface, reflectance. This is particularly critical because atmospheric gases such as  $O_2$ ,  $O_3$ ,  $CO_2$ , and  $H_2O$  produce distinct absorption features that can be mistaken for surface material signatures if left uncorrected (Jensen, 2016; Richards, 2022). While multispectral instruments are often designed with bands that avoid major absorption features, hyperspectral sensors measure across the full spectrum, making them especially sensitive to atmospheric effects. Figures 11 and 12 illustrate these absorption features, emphasizing the need for correction to avoid misinterpretation.

When dedicated atmospheric correction software such as MODTRAN or FLAASH is not available, simplified approaches known as vicarious calibration may be employed. These methods use ground reference targets or invariant features to approximate corrections. Although they do not allow for strict wavelength-by-wavelength comparison between remote sensing and laboratory spectra, they can still provide sufficiently accurate reflectance estimates for identifying major spectral features and distinguishing materials in a scene (Clark et al., 2003; Thenkabail & Lyon, 2016).

## 3.2. Fundamental Analysis Methods

Once atmospheric and geometric corrections are completed, defective bands masked, and optional dimensionality reduction applied, the next step is to extract information from hyperspectral datasets (Richards, 2022). A central challenge is that while some pixels represent relatively “pure” spectra of single materials, most pixels are mixed or noisy, reflecting contributions from multiple sources (Goetz et al., 1985). The analysis therefore



begins with the identification of representative “endmember” spectra, typically the purest or most characteristic pixels in a scene (Boardman, 1993). These endmembers are then compared with spectral libraries or field measurements to establish their material identity (Clark et al., 2003), after which their distribution can be mapped across the dataset (van der Meer et al., 2012). This process is inherently iterative: initial hypotheses about endmembers are refined through repeated inspection, comparison, and mapping until a consistent interpretation emerges (Plaza et al., 2011). The outcome of such analysis is usually documented with maps of sampled locations, spectral plots with reference comparisons, and thematic or abundance maps showing the extent of identified materials (Bioucas-Dias et al., 2012).

#### Typical workflow:

- Identification of representative pixels with relatively pure spectra (Boardman, 1993).
- Extraction and visualization of these spectra (“endmember collection”) (Plaza et al., 2011).
- Comparison with laboratory or field spectral libraries (Clark et al., 2003).
- Mapping the spatial distribution of pixels similar to the endmembers (van der Meer et al., 2012).
- Iterative refinement and validation of endmember selection and results (Bioucas-Dias et al., 2012).

### 3.3. Principles of Spectral Indices

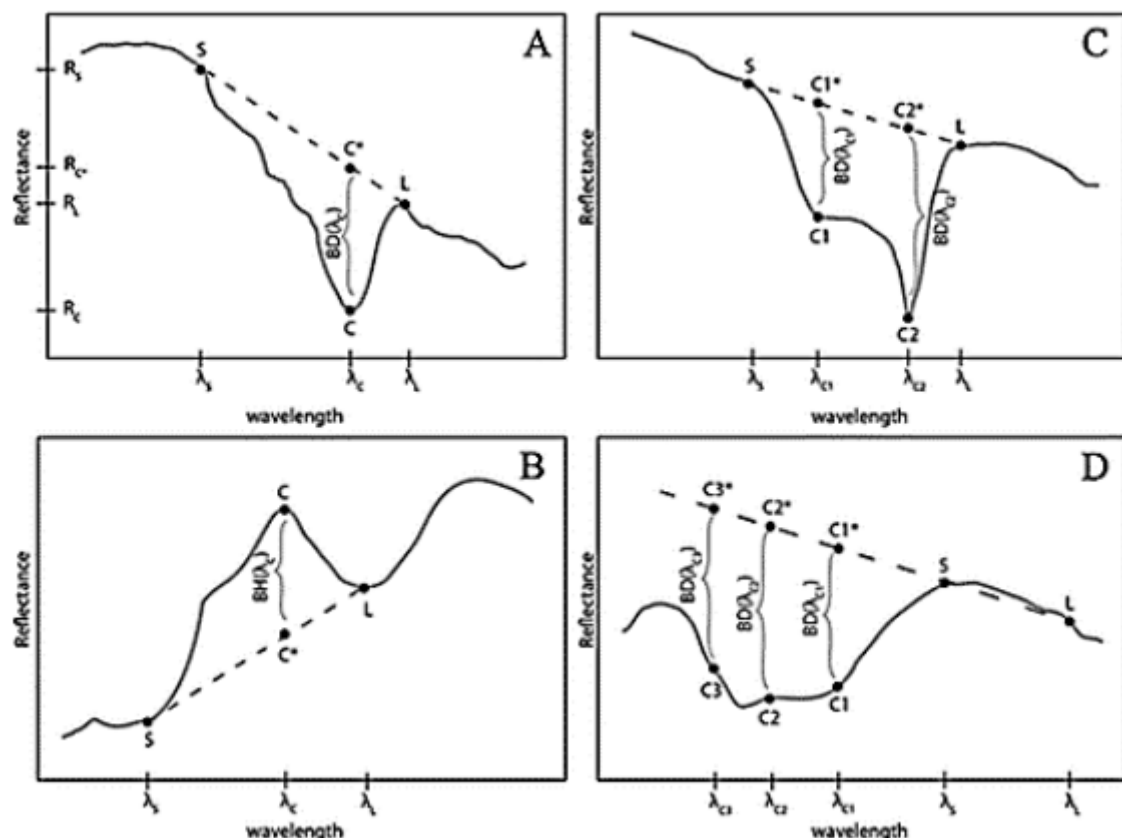


Figure 13: Variations of spectral indices calculation to measure specific features of the spectra (Viviano et al., 2014)

Spectral indices are mathematical combinations of selected spectral bands designed to enhance specific properties of the Earth's surface. They provide simplified, but powerful tools to interpret complex reflectance behavior by highlighting differences between spectral regions that are sensitive to vegetation, water, or disturbance. The most prominent of these is the Normalized Difference Vegetation Index (NDVI), introduced by Tucker in 1979, which exploits the strong absorption of red light by chlorophyll and the high reflectance of near-infrared light by plant cell structure. NDVI values close to one indicate dense, healthy vegetation, while values near zero or negative correspond to sparse vegetation, soil, or water (Tucker, 1979).

Two widely used indices share the acronym NDWI: the green-NIR NDWI for open-water detection (McFEETERS, 1996) and the NIR-SWIR NDWI for vegetation liquid water content (Gao, 1996). While the Normalized Burn Ratio (NBR) exploits shortwave infrared bands to identify burned areas and assess fire severity (Key & Benson, 2006). The Modified Soil Adjusted Vegetation Index (MSAVI) accounts for soil reflectance effects in sparsely vegetated areas (Qi et al., 1994), improving sensitivity in arid landscapes. In hyperspectral datasets, more specialized indices target narrow absorption features, such as the Photochemical Reflectance Index (PRI) for photosynthetic efficiency (Gamon et al., 1992) or red-edge indices for chlorophyll concentration (Delegido et al., 2011; Gamon et al., 1992).

The value of indices lies in their computational simplicity and their ability to transform raw reflectance data into meaningful biophysical proxies. They are essential for global vegetation monitoring, drought detection, deforestation mapping, and agricultural yield estimation. However, indices are also subject to limitations. Atmospheric interference, sensor calibration, and saturation effects in dense vegetation can affect reliability. Despite these challenges, spectral indices remain among the most widely used tools in remote sensing (van der Meer et al., 2012).

### 3.4. Spectral Similarity and Unmixing Approaches

Beyond the use of spectral indices that target specific absorption features, hyperspectral analysis often requires algorithms that can handle high-dimensional data and mixed spectra (Richards, 2022). Two widely applied approaches are the Spectral Angle Mapper (SAM) and Linear Spectral Unmixing (LSU) (Kruse et al., 1993).

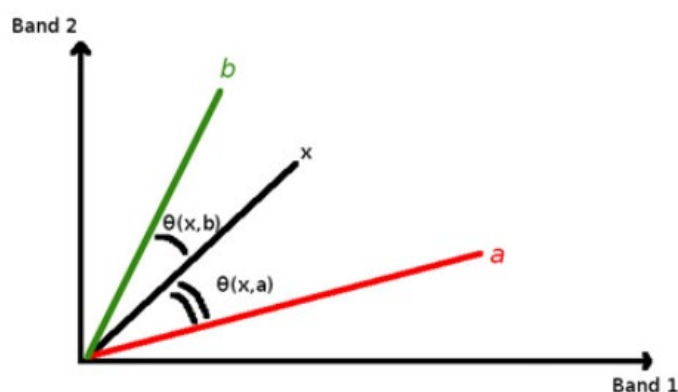


Figure 14: Principle of SAM: An unclassified point in feature space ( $x$ ) will be assigned to that class to which it has the smallest spectral angle (here:  $b$ ) (Spectral Angle Mapper Processor - ESA, n.d.)

The Spectral Angle Mapper is a geometry-based classification technique (Kruse et al., 1993). Instead of using Euclidean distances between spectral vectors, SAM measures the angle between the vector representing the unknown pixel spectrum and a reference endmember spectrum in multi-dimensional feature space (Boardman, 1993). This angle is invariant to multiplicative scaling, meaning that variations in brightness caused by topographic shading or illumination changes do not affect the result. Pixels are assigned to the class of the reference spectrum with which they form the smallest spectral angle (Kruse et al., 1993). SAM is computationally efficient, requires only a set of reference endmembers, and is particularly robust in scenes with strong illumination variability (Richards, 2022). However, its reliance on spectral angle alone can sometimes lead to confusion between spectrally similar but distinct materials, so its results are often cross-validated with other methods or direct spectral inspection (Plaza et al., 2011).

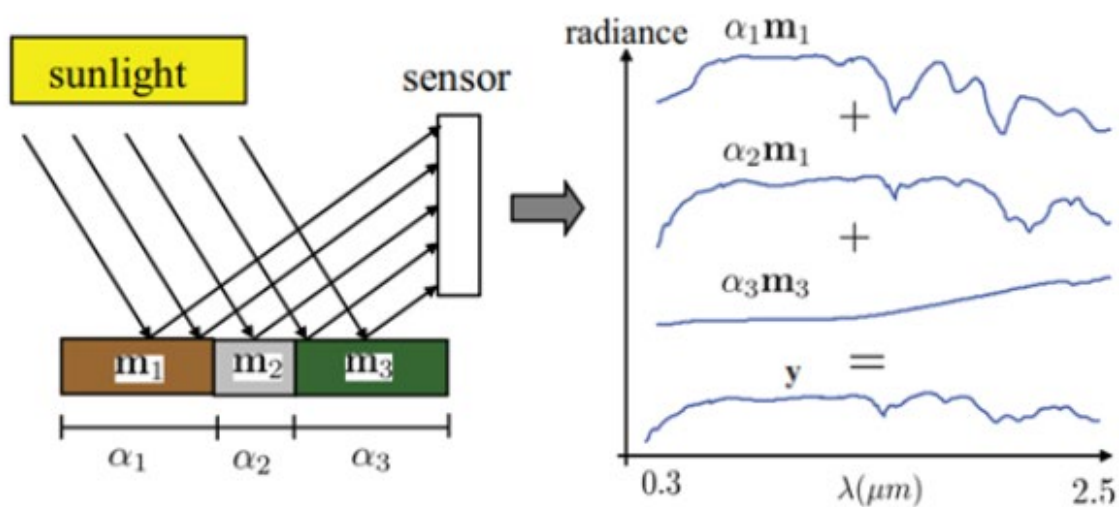


Figure 15: Principle of linear mixtures (Bioucas-Dias et al., 2012)

#### Constraints applied in LSU include:

- **Nonnegativity:** No endmember can have a negative fraction. A negative abundance would be physically meaningless, equivalent to inverting the spectrum (Bioucas-Dias et al., 2012).
- **Sum-to-one:** Endmember fractions should add up to 100% of the pixel. In some cases, this constraint is relaxed (e.g., to allow for unknown materials not in the endmember set), and the sum may be  $< 1$  (Heinz & Chein-I-Chang, 2001).
- **Limited number of endmembers per pixel:** To improve interpretability, the number of endmembers allowed in any given pixel may be constrained (e.g., max 3). The algorithm then tests all possible ternary mixtures from the collection, finds the best fit, and outputs abundances and errors. This avoids unrealistic mixtures of a large number of materials and has been shown to improve results in both terrestrial and planetary studies (Bioucas-Dias et al., 2012).

Linear Spectral Unmixing, in contrast, assumes that each pixel's reflectance spectrum can be modeled as a weighted linear combination of a limited set of endmember spectra (Adams et al., 1986). The task is to solve the linear system of equations that represents this mixing model, with constraints such as non-negativity (endmember abundances cannot be negative) and sum-to-one (fractions add to 100%) (Bioucas-Dias et al., 2012). This yields fractional

abundance maps for each material, providing quantitative estimates of sub-pixel composition (Adams et al., 1986). Advanced implementations allow for relaxing constraints (e.g., sum-to-one  $< 1$  to accommodate unknown endmembers) or limiting the number of endmembers per pixel to improve interpretability (Heinz & Chein-I-Chang, 2001). LSU is particularly powerful in geological and planetary applications, where mixed pixels dominate due to coarse spatial resolution (Goetz et al., 1985). Its computational complexity is higher than SAM, but it provides richer quantitative information about material abundances rather than simple class labels (Bioucas-Dias et al., 2012).

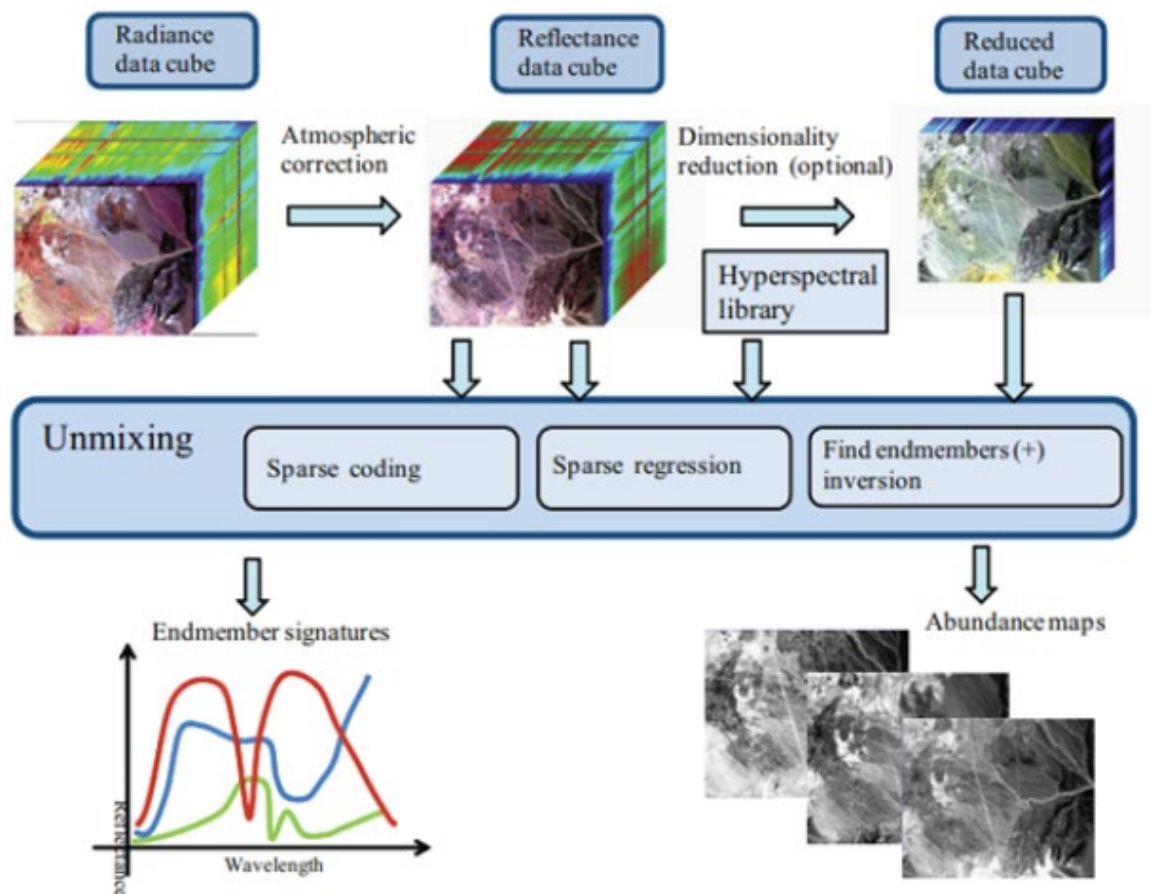


Figure 16: Complete pathway from raw data to results, using spectral unmixing (Bioucas-Dias et al., 2012)

SAM and LSU represent complementary strategies: SAM emphasizes efficient similarity-based classification that is robust to illumination effects, while LSU provides a physically grounded approach to quantifying mixture fractions within pixels (Plaza et al., 2011). In combination, they offer a strong analytical toolkit for deriving both qualitative and quantitative information from hyperspectral remote sensing data (Bioucas-Dias et al., 2012).

## 4. Active Sensors

Active remote sensing systems are characterized by the fact that they transmit their own energy towards the Earth and record the response that is scattered back. This fundamental capability allows them to operate independently of solar illumination, in both daytime and nighttime, and to penetrate through clouds, haze, and even smoke, which typically limits passive systems (James B. Campbell & Randolph H. Wynne, 2011; Woodhouse, 2017). Radar is the most widely used active sensing technology for Earth observation, operating in the microwave region of the spectrum, although lidar, which uses laser pulses in the visible or near-infrared range, is also a prominent active technique, particularly for Digital Surface Models (DSM), Digital Elevation Models (DEM), topographic mapping and vegetation structure analysis (Jensen, 2016).

Radar's strength lies in its sensitivity to surface roughness, moisture content, and dielectric properties of the target. Its evolution has been shaped by early military applications and subsequently adapted for Earth observation. The first radar systems, built in the 1930s and 1940s, demonstrated the ability to detect objects at distance using radio waves (Watson-Watt, 1946), but it was not until the development of side-looking airborne radar (SLAR) systems in the 1950s that consistent radar imaging of the Earth's surface became possible (Moreira et al., 2013). Lidar, in contrast, transmits laser pulses and measures the time delay of their return, providing extremely high vertical resolution measurements of canopy structure and terrain elevation (James B. Campbell & Randolph H. Wynne, 2011). While lidar has limited spatial coverage from satellite platforms, it has become indispensable in airborne campaigns. Radar, with its global coverage from satellites, has therefore become a cornerstone of modern Earth observation (Meyer, 2019).



## 4.1. Basic Principles of Radar



Figure 17: Radar of the type used for detection of aircraft. It rotates steadily, sweeping the airspace with a narrow beam. Air Force Museum, Hatzerim, Israel. Source: [Wikipedia](https://en.wikipedia.org/wiki/Parabolic_reflector_antenna)

Radar, an acronym for “RADio Detection And Ranging”, is an active remote sensing system that operates by transmitting microwave pulses and recording the portion of energy that is scattered back from the Earth’s surface. In contrast to passive optical sensors that rely on reflected solar energy, radar generates its own illumination, making it independent of sunlight and largely unaffected by clouds, haze, or smoke. This ability to provide consistent day-and-night, all-weather observations is the main reason why radar became a cornerstone of Earth observation during the late twentieth and early twenty-first centuries (Flores et al., 2019; Woodhouse, 2017).

The origins of radar lie in early twentieth century experiments with radio waves and their reflection from metallic objects. During the 1930s and 1940s, radar was rapidly developed for military applications such as aircraft detection and navigation, with early pioneers like Robert Watson-Watt laying the groundwork for operational radar systems (Watson-Watt, 1946).

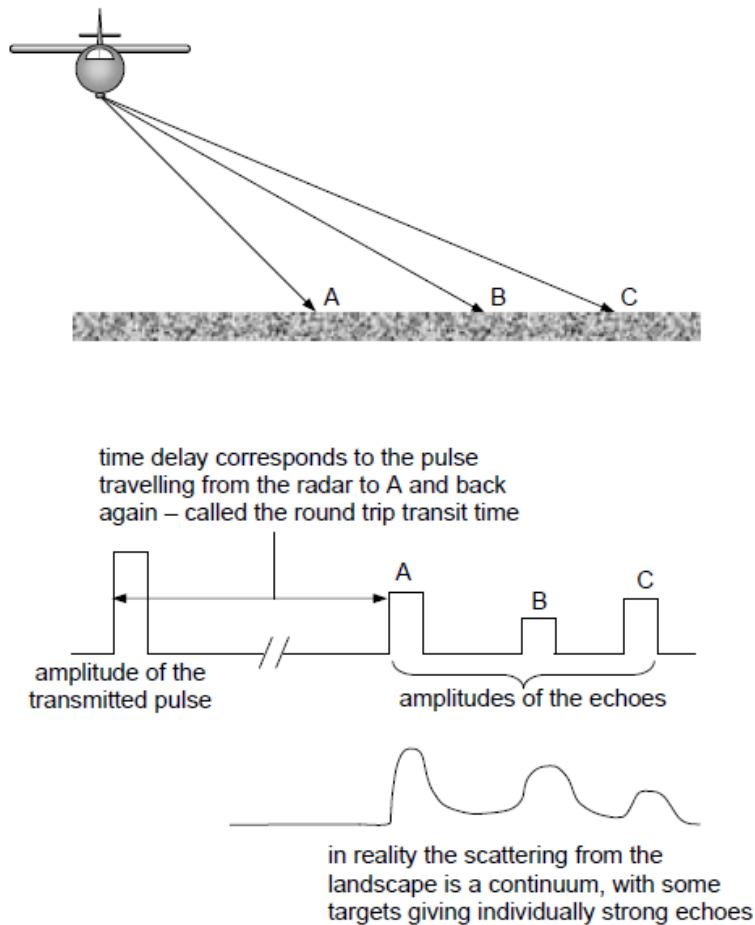


Figure 18: Side Looking Radar: Resolution of targets spatially by time resolution of the received echoes. (Richards, 2009)

After World War II, radar technology was adapted to scientific purposes, including meteorological observations and geoscience. Airborne radar systems were introduced in the 1950s, using side-looking geometries to generate continuous strips of ground imagery. These systems, known as Side-Looking Airborne Radar (SLAR), were the first to deliver consistent radar images of the Earth's surface. However, their azimuth resolution was fundamentally limited by antenna size: the longer the antenna, the better the resolution, which became impractical for higher altitudes (Richards, 2009).

The breakthrough came with the principle of synthetic aperture. By exploiting the motion of the radar platform along its flight path and combining the phase history of the received echoes, it became possible to synthesize the effect of a very long antenna, dramatically improving azimuth resolution. This development gave rise to Synthetic Aperture Radar (SAR), which remains the dominant form of radar imaging today (Moreira et al., 2013). The first demonstrations of spaceborne SAR occurred with the launch of NASA's Seasat in 1978. Despite its short lifetime, Seasat proved the feasibility of acquiring global radar imagery from orbit and set the stage for future satellite programs. The 1990s saw the deployment of dedicated Earth observation SAR missions such as ESA's ERS-1 and ERS-2, and Canada's Radarsat-1, which enabled systematic environmental monitoring.

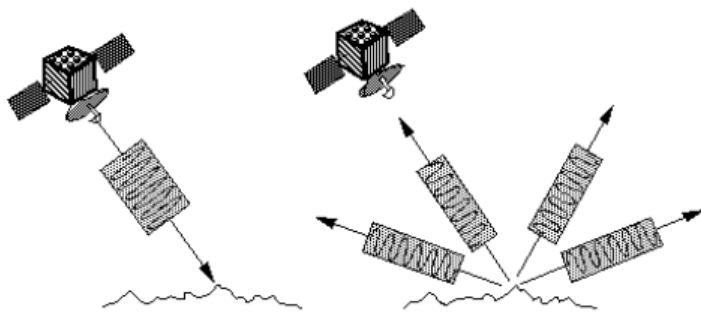


Figure 19: Echoes received back by the Antenna (European Space Agency, 2007)

In the twenty-first century, SAR missions have matured into global operational systems. The European Space Agency's Sentinel-1 constellation, launched in 2014 and 2016, represents the current state of the art. Operating at C-band with a wide swath and regular revisit times, Sentinel-1 provides freely accessible data that supports a wide range of applications, from land cover monitoring and hazard mapping to ice dynamics and infrastructure stability. These missions illustrate the continuity of radar's basic principles: transmitting microwave pulses, recording backscattered energy, and using system geometry and wavelength to capture information about the Earth's surface (Torres et al., 2012).

## 4.2. Sidelooking Radar

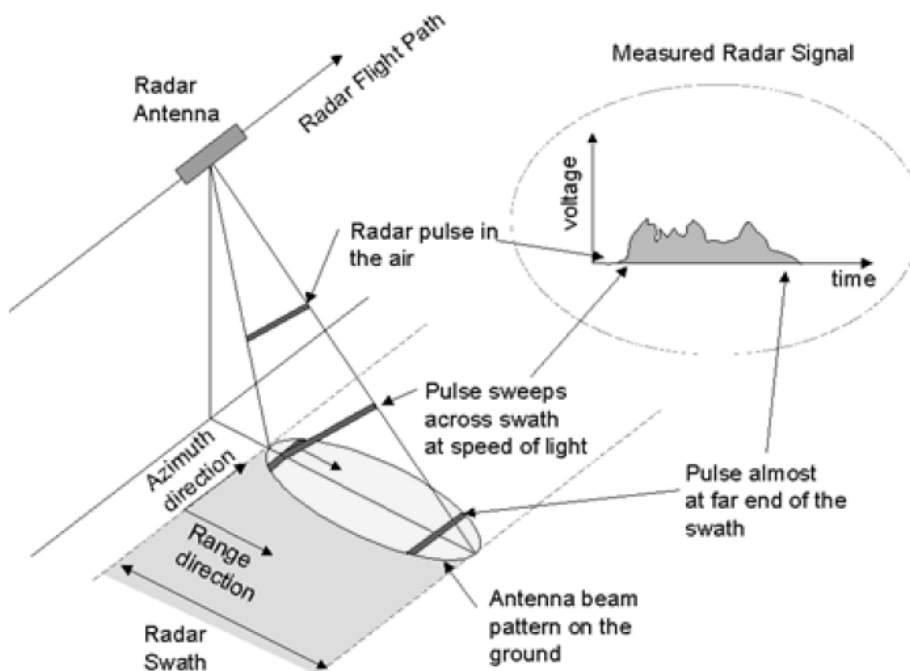


Figure 20: Imaging geometry for a side-looking radar system (Van Zyl & Kim, 2011)

Side-looking airborne radar represented the first significant leap in radar imaging. In such systems, an antenna mounted on an aircraft transmitted pulses obliquely to the ground, and the backscattered signals were used to form images. However, the resolution of SLAR was inherently constrained by the length of the antenna: as altitude increased, the size of the

footprint widened, leading to reduced azimuth resolution. This limitation made it impractical for high-resolution imaging from spaceborne platforms.

## 4.3. Synthetic Aperture Radar (SAR)

### 4.3.1. Introduction to SAR: From Radar to SAR

The practical birth of the synthetic aperture is attributed to Carl Wiley's synthetic aperture principle, first patented in 1952, which established the foundation for the modern digital processing lineage (Cumming & Wong, 2005). Wiley recognized that the Doppler frequency shifts produced as the radar platform moved along its flight path could be exploited to synthetically extend the effective antenna length. By coherently combining the returns from many successive pulses, a "synthetic" long antenna was formed, enabling much finer azimuth resolution than physically possible with the onboard antenna alone (Cumming & Wong, 2005). This principle laid the foundation for Synthetic Aperture Radar (SAR).

The first spaceborne SAR was launched on NASA's Seasat satellite in 1978. Despite its short operational period of 106 days, Seasat demonstrated the potential of SAR for global ocean and land monitoring. In the following decades, a series of missions established the global SAR constellation: ESA's ERS-1 (1991) and ERS-2, Canada's Radarsat series, Japan's ALOS PALSAR missions, and ESA's Sentinel-1 program, which since 2014 has provided continuous, open-access C-band SAR data. Together these missions have created a dense archive that allows systematic monitoring of Earth's surface regardless of atmospheric conditions (Flores et al., 2019).

### 4.3.2. Doppler Effect.

The Doppler effect describes the change in frequency of a wave due to relative motion between the source and the receiver: frequencies increase as the sensor approaches the target and decrease as it moves away. In synthetic aperture radar (SAR), this frequency shift is exploited by coherently combining echoes from successive positions along the flight path. By processing signals across these varying Doppler frequencies, a synthetic antenna aperture much longer than the physical antenna is formed, thereby improving azimuth resolution and reducing the effective ground pixel size (Cumming & Wong, 2005; Moreira et al., 2013).

### 4.3.3. SAR Frequency Bands and Applications

SAR instruments operate across different frequency bands in the microwave spectrum, each with distinct penetration capabilities and applications. X-band, with wavelengths of about 2.4-3.8 cm, provides very high spatial resolution and is suitable for urban monitoring and infrastructure studies but penetrates poorly into vegetation. C-band, with wavelengths of about 3.8-7.5 cm, has been the workhorse of SAR remote sensing for decades, balancing spatial resolution, canopy penetration, and wide-swath imaging, as exemplified by Sentinel-1. L-band, with wavelengths of about 15-30 cm, penetrates deeply into vegetation canopies and is indispensable for biomass estimation, forest monitoring, and subsurface detection in dry soils. P-band, with wavelengths of 30-100 cm, penetrates even further, making it suitable for measuring forest structure and biomass, though it suffers from ionospheric distortions and



has not yet been widely implemented in spaceborne missions. ESA's upcoming Biomass mission will be the first to provide global P-band SAR observations (Moreira et al., 2013).

Name	Wavelength	Example of sensors	Example of typical applications
P-band	~ 65 cm	Biomass	First P-band spaceborne; vegetation mapping and assessment
L-band	~ 23 cm	ALOS PALSAR, NISAR	Medium resolution SAR (geophysical monitoring; biomass and vegetation mapping; high penetration, InSAR)
S-band	~ 10 cm	NISAR	Agriculture monitoring, higher vegetation density
C-band	~ 5 cm	ERS-1/2 SAR, RADARSAT-1/2, ENVISAT ASAR, RISAT-1, Sentinel-1	SAR Workhorse (global mapping; change detection; monitoring of areas with low to moderate penetration; higher coherence); ice, maritime ocean navigation
X-band	~ 3 cm	TerraSAR-X, COSMO-SkyMed, Capella, ICEYE	High-resolution SAR (urban monitoring; ice and snow, little penetration into vegetation cover; fast coherence decay in vegetated areas)
K-band	~ 1.2 cm	-	Primarily climate & atmosphere-related applications. Also military domain applications, e.g., surveillance

Table 2: SAR Bands (Flores et al., 2019) as well as internet research on K-band.

#### 4.3.4. Reflection

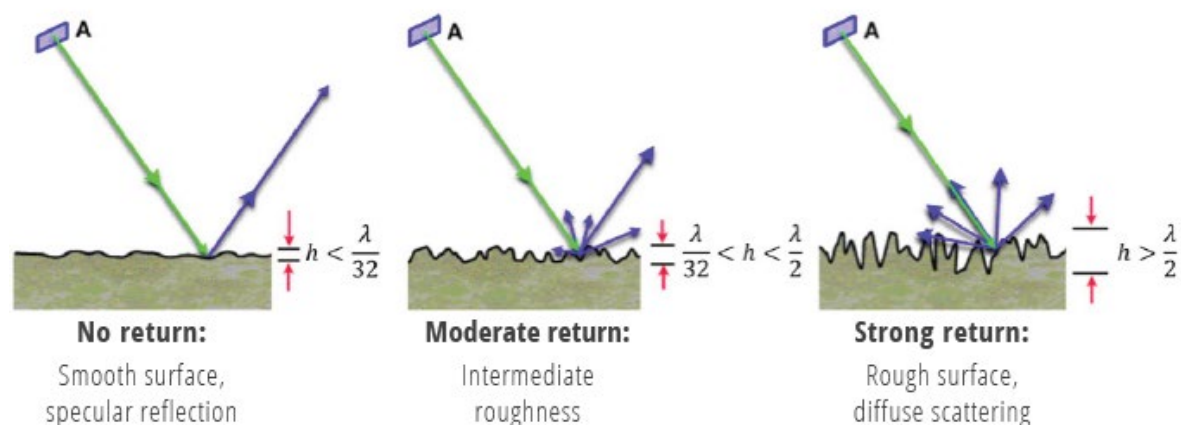


Figure 21: Conceptual sketch of the dependence of surface roughness on the sensor wavelength  $\lambda$ : (a) smooth, (b) intermediate, and (c) rough. (Flores et al., 2019)

In RADAR but also in Synthetic Aperture Radar (SAR), the strength and characteristics of the reflected signal depend on the interaction between the transmitted microwave pulse and the surface geometry, roughness, and dielectric properties of the target. Smooth surfaces, such as calm water, tend to reflect energy away from the sensor, appearing dark, while rough surfaces or complex scatterers reflect energy back, producing bright returns. Urban structures often generate strong reflections through double-bounce mechanisms, while vegetation canopies produce volume scattering. Because SAR coherently records both amplitude and



phase of the backscattered signal, these reflections not only form the basis of image intensity but also enable advanced techniques such as interferometry and polarimetry, extending the information beyond what is possible with optical imagery (Flores et al., 2019; Richards, 2009; Van Zyl & Kim, 2011; Woodhouse, 2017).

#### 4.3.5. Geometric Distortions

SAR images are also subject to geometric distortions inherent to the side-looking imaging geometry. Foreshortening occurs when terrain slopes facing the sensor appear compressed, layover occurs when tall features are imaged before their base, and radar shadows appear when steep terrain obstructs illumination. These distortions can be mitigated through the use of digital elevation models for geometric correction (Flores et al., 2019; Meyer, 2019; Richards, 2009).

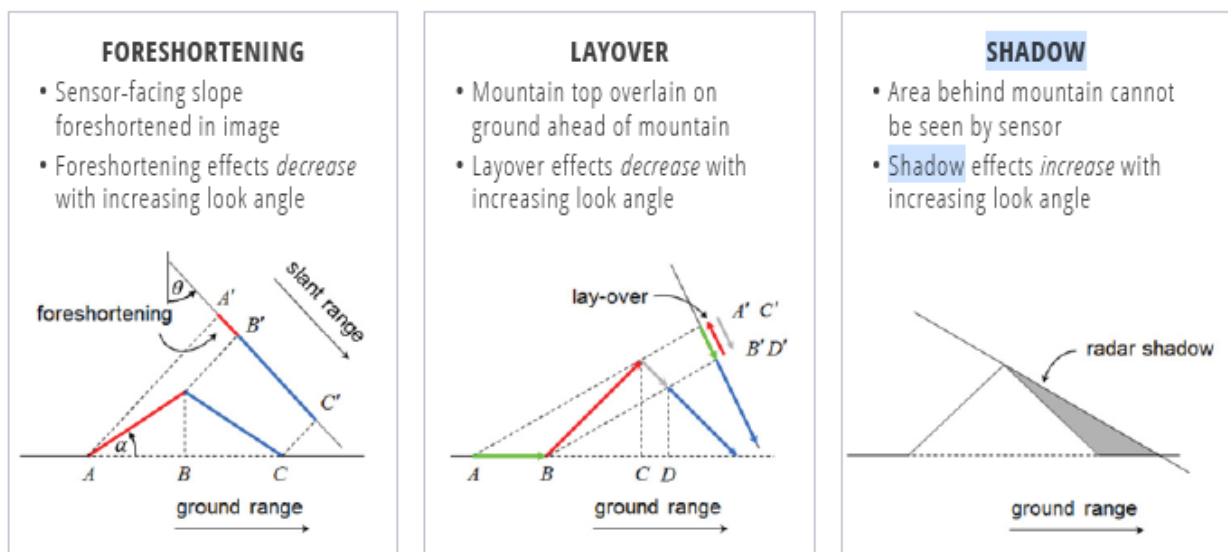


Figure 22: Main geometric distortions on SAR images with their dependence on acquisition geometry: (a) foreshortening, (b) layover, and (c) shadow. (Flores et al., 2019)

#### 4.3.6. Penetration

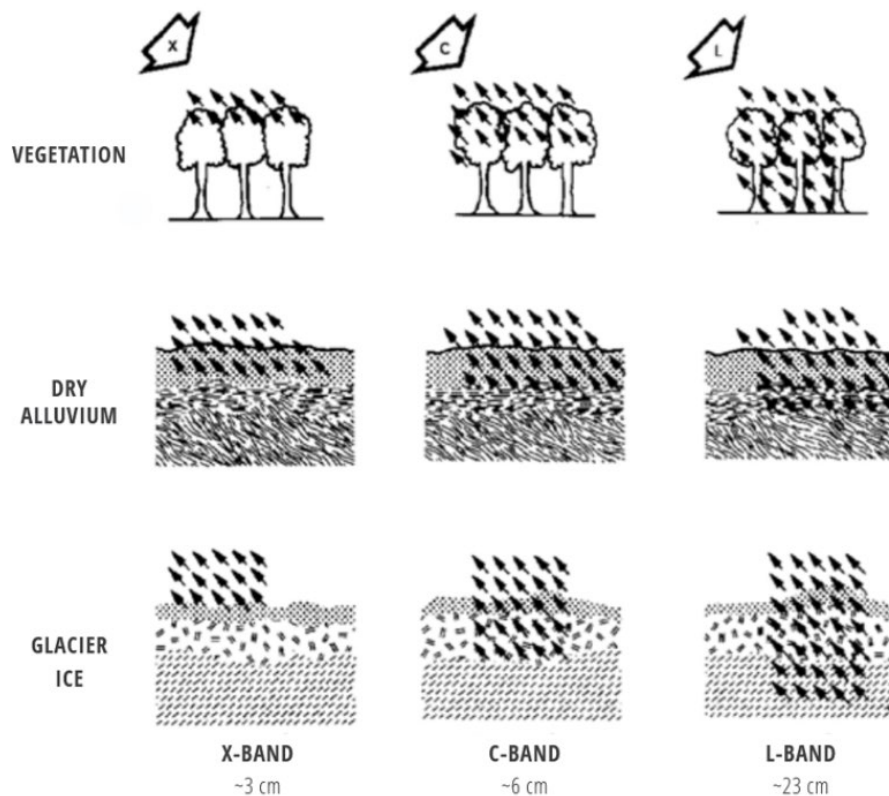


Figure 23: Penetration of different wavelengths for different materials (Meyer, 2019)

The ability of Synthetic Aperture Radar (SAR) to penetrate different media is governed primarily by its wavelength, polarization, and the dielectric properties of the target. Longer wavelengths, such as L-band (15-30 cm) and P-band (30-100 cm), penetrate more deeply into vegetation canopies and dry soils compared to shorter X-band (2-4 cm) systems, which are largely confined to surface interactions (Flores et al., 2019; Moreira et al., 2013; Woodhouse, 2017). In vegetated areas, L-band and P-band signals can interact with trunks and larger branches, making them particularly useful for forest structure and biomass estimation (Flores et al., 2019). In soil penetration depth is strongly reduced by increasing moisture content, as water has a high dielectric constant and strongly absorbs microwave energy. Snow and dry sand allow relatively deep penetration, while wet snow, water surfaces, or saturated soil appear dark due to strong absorption and specular reflection. This property makes SAR valuable for applications such as subsurface soil moisture retrieval, flood mapping beneath vegetation, and monitoring of permafrost and ice structures (Flores et al., 2019; Ulaby et al., 1981; Woodhouse, 2017).

#### 4.3.7. Polarization

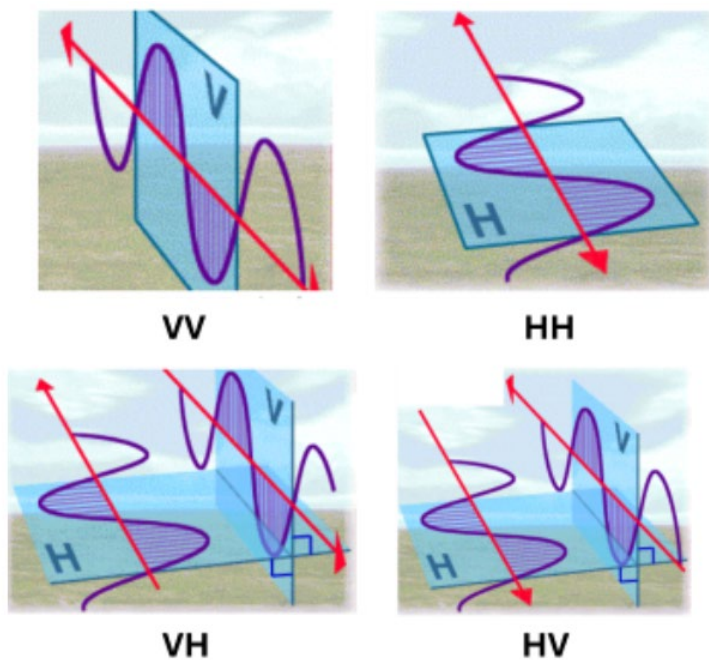


Figure 24: : Polarization of sent and received waves (based on images from ESA) (European Space Agency, 2007)

Polarization represents another critical dimension of radar measurements. Most modern synthetic aperture radar (SAR) systems can transmit and receive in horizontal (H) or vertical (V) polarization. The four possible combinations—HH, HV, VH, and VV—provide complementary information about scattering mechanisms. Co-polarized channels (HH, VV) are typically associated with surface scattering and double-bounce effects, whereas cross-polarized channels (HV, VH) are more sensitive to volume scattering, especially within vegetation canopies (Flores et al., 2019; Richards, 2022; Van Zyl & Kim, 2011).

Single polarization	HH or VV
Single polarization	HH or VV
Dual polarization	HH + HV, or VV + VH, or HH + VV
Alternating polarization	HH + HV, alternating with VV + VH
Polarimetric (Quad-pol)	HH, VV, HV, VH

Table 3: Possible polarisation modes (European Space Agency, 2007)

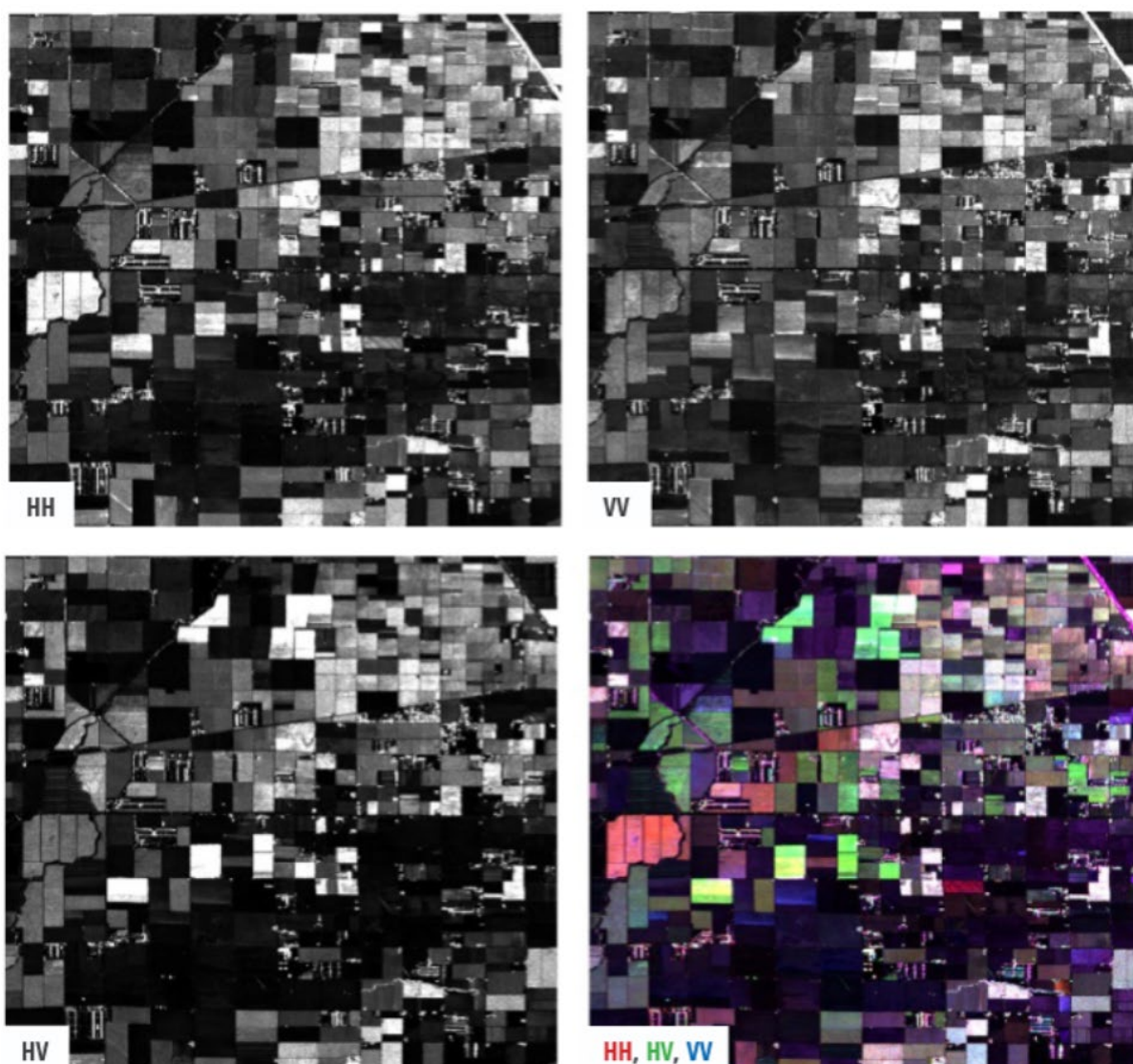


Figure 25: Illustration of how different polarizations (HH, VV, HV, and color composites) bring out different features in an agricultural scene from California's Central Valley. The different orchards and crops in this area display different polarized backscatter behavior (Flores et al., 2019, p. 219)

#### 4.3.8. Speckle

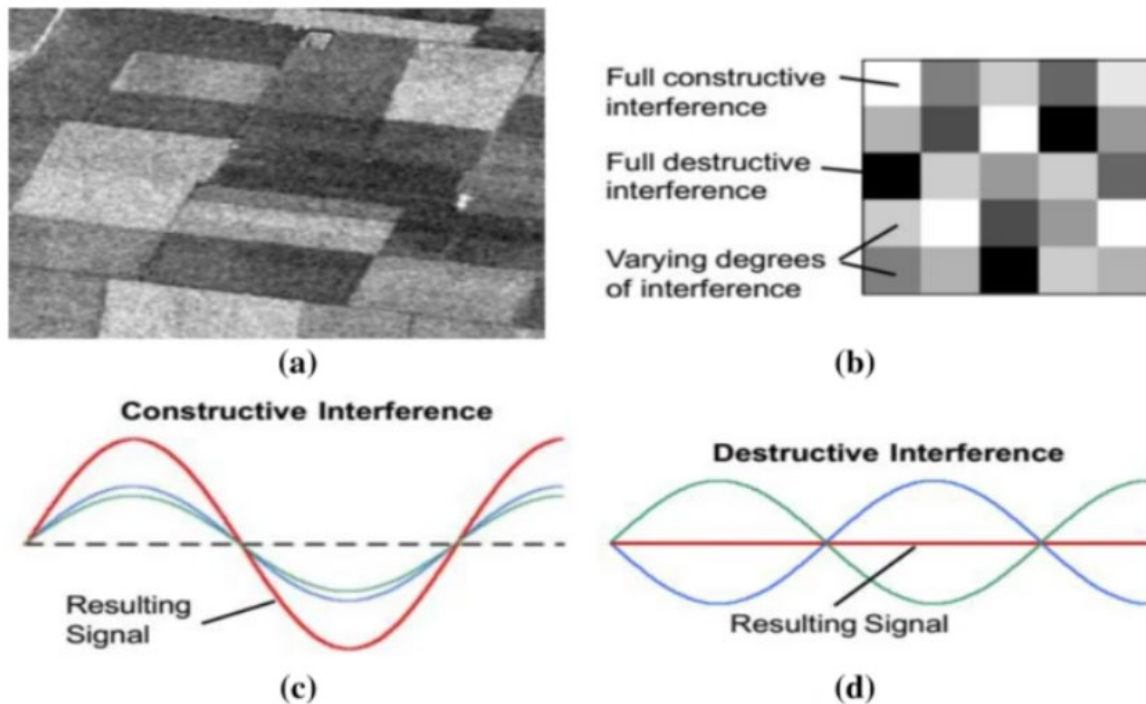


Figure 26: Illustration of the speckle effect from Singh et al. (2021). (a) Agricultural fields showing a grainy texture caused by (c) constructive and (d) destructive interference of backscattered waves (b).

A distinctive characteristic of Synthetic Aperture Radar (SAR) imagery is speckle, a granular texture caused by the coherent interference of electromagnetic waves scattered from multiple elementary scatterers within a resolution cell. Speckle is multiplicative in nature, typically modeled by an exponential distribution, and while it contains statistical information about the scattering medium, it complicates visual interpretation and quantitative analysis (J. S. Lee et al., n.d.; J.-S. Lee, 1980; Woodhouse, 2017). As a result, speckle reduction is a crucial preprocessing step in SAR analysis.

Several filtering strategies have been developed to address speckle. Classical approaches include adaptive filters, such as the Lee filter (J.-S. Lee, 1980) and the Frost (Frost et al., 1982), which locally estimate backscatter statistics to smooth noise while preserving edges. Another well-established method is multilooking, which averages independent looks of the same scene to reduce speckle variance. This improves radiometric accuracy but reduces spatial resolution, making the method most suitable for classification and interpretation tasks (J. S. Lee et al., n.d.; Richards, 2009).

More recent approaches exploit the structural redundancy of images. The non-local means (NLM) filter compares patches across the image and averages only statistically similar ones, thereby reducing speckle variance while preserving fine details and edges (Small, 2011). Building on this concept, Deledalle et al. (2009) proposed an iterative weighted maximum likelihood extension of NLM, in which patch similarity is defined statistically according to the underlying noise distribution rather than simple Euclidean distance. By iteratively refining weights using both noisy and estimated patches, this method achieves superior denoising performance for low signal-to-noise ratio images, particularly in synthetic aperture radar (SAR) data affected by multiplicative speckle noise (Deledalle et al., 2009).



### 4.3.9. Backscattering

Backscattering in SAR imagery refers to the portion of the transmitted microwave pulse that is scattered back to the sensor after interacting with the Earth's surface. The magnitude and polarization of this return signal depend on the geometry, dielectric properties, and roughness of the target. Strong HH backscatter is often associated with double scattering, where man-made objects such as buildings or ships produce bright returns due to efficient corner reflector geometries. Strong VV backscatter generally arises from surface scattering on rough surfaces such as bare soils or disturbed water, while strong VH responses are characteristic of volume scattering, which occurs within vegetation and forest canopies. These distinctions form the foundation of SAR interpretation, linking physical scattering mechanisms to image signatures (Richards, 2009; Woodhouse, 2017).

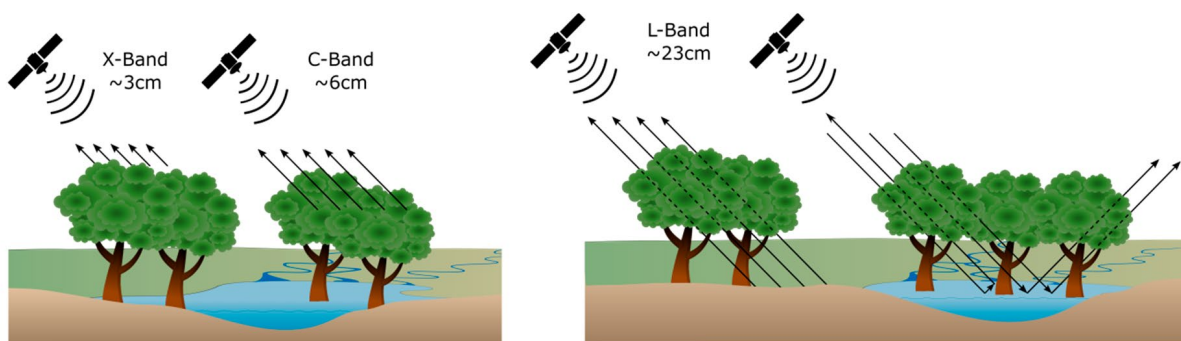


Figure 27: Radar backscattering mechanisms for different SAR wavelengths: X- and C-band (left) and L-band (right) (Ottinger & Kuenzer, 2020)

#### 4.3.9.1. RCS

The strength of the backscatter is commonly expressed as the radar cross section (RCS). RCS is influenced by several factors: surface roughness relative to the radar wavelength, the dielectric constant of the target, the incidence angle of the radar beam, and the geometric arrangement of scatterers. Additionally, radar wavelength strongly affects the penetration depth: longer wavelengths such as L- or P-band penetrate more deeply into vegetation canopies and dry soils, while shorter X-band wavelengths interact mainly with fine-scale features like leaves and small branches (Moreira et al., 2013; Richards, 2022; Woodhouse, 2017).

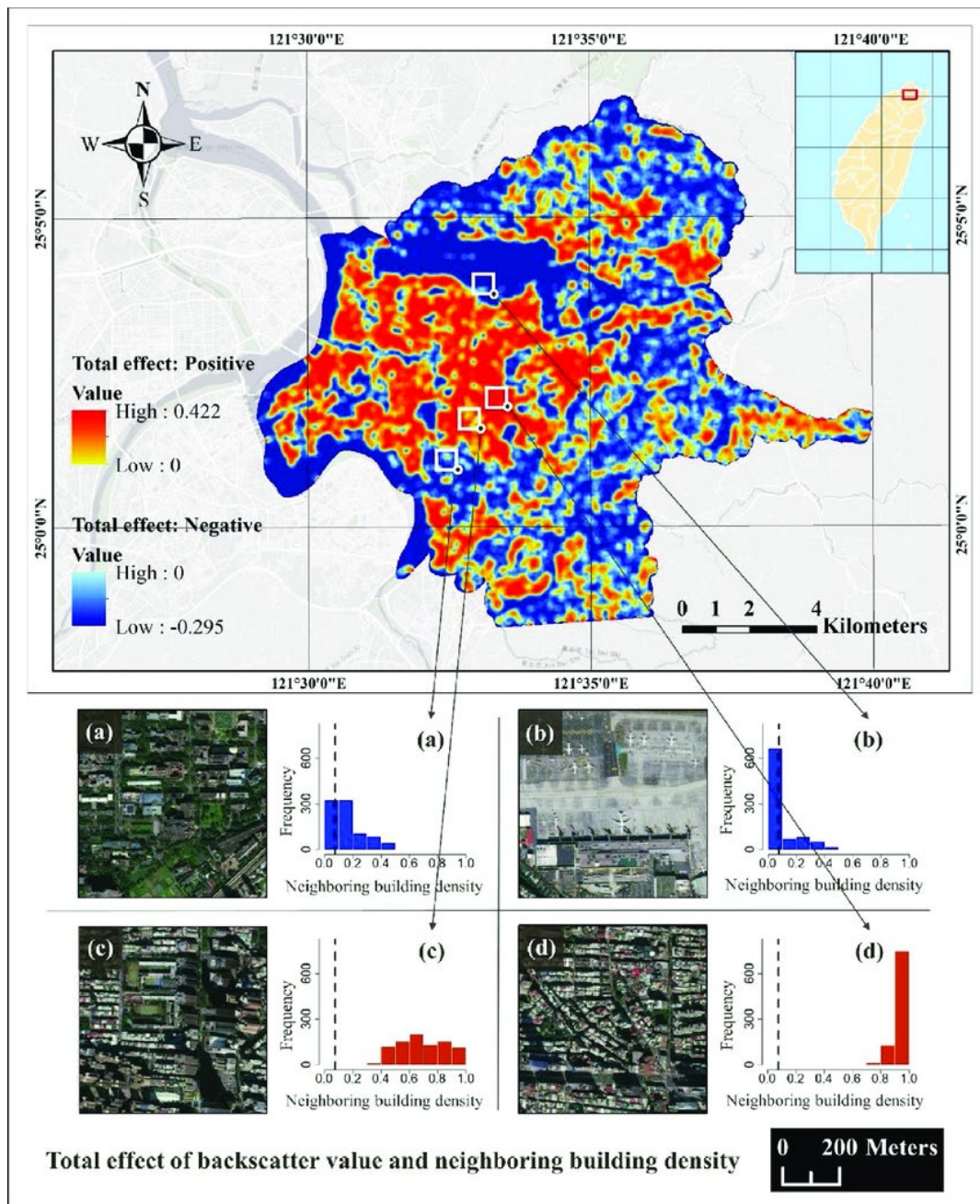


Figure 28: Backscatter: Total effect of the backscatter values in urban detection (Liao & Wen, 2020)

#### 4.3.9.2. Scattering Types

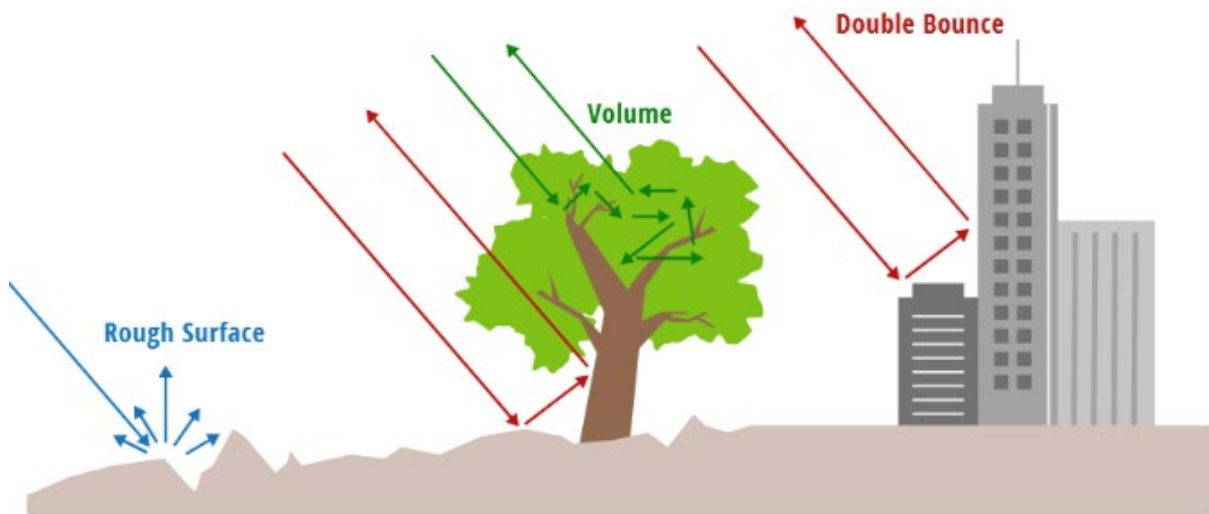


Figure 29: Illustration of main scattering types for SAR data (Meyer, 2019)

##### 4.3.9.2.1. Specular Scattering

Specular scattering occurs when radar waves strike a surface that is smooth relative to the radar wavelength. In this case, most of the energy is reflected away from the sensor, producing very low backscatter. Examples include calm water bodies and smooth asphalt surfaces, which typically appear dark in SAR imagery (Meyer, 2019) (Meyer, 2019).

##### 4.3.9.2.2. Diffuse Scattering

As surface roughness increases relative to the wavelength, scattering becomes diffuse, with energy distributed in multiple directions. Diffuse scattering produces stronger radar returns and is characteristic of surfaces such as bare soils, agricultural fields, or disturbed water (Meyer, 2019; Richards, 2009).

##### 4.3.9.2.3. Volume Scattering

Volume scattering arises when radar waves penetrate into a medium and undergo multiple reflections before returning to the sensor. This process is common in vegetation, where leaves, twigs, and trunks scatter the radar signal in many directions, and in snow or soil composed of fine particles. Volume scattering is typically associated with cross-polarized returns (VH or HV), making it particularly important for forest and vegetation studies (Flores et al., 2019).

#### 4.3.9.2.4. Double-Bounce Scattering

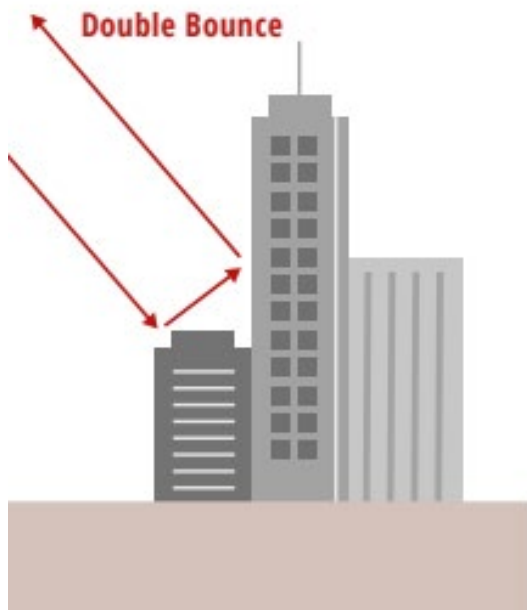


Figure 30: Double Bounce (Flores et al., 2019, p. 28)

A particular case of specular reflection in radar remote sensing is the so-called double-bounce scattering. In this phenomenon, the transmitted wave undergoes two reflections before returning to the sensor: typically, a vertical structure (such as a building wall or tree trunk) and an adjacent horizontal surface (such as the ground or calm water) form a near-orthogonal corner reflector. The wave is first reflected from one surface and then specularly from the second, after which it is directed back toward the antenna. Because of the geometry, this type of scattering is highly efficient, often producing strong returns that dominate the radar backscatter in urban environments or other areas with man-made infrastructure. Double-bounce signatures are easily recognizable in SAR images of cities, ports, and ships, where vertical walls and flat surfaces interact to create bright scatterers (Van Zyl & Kim, 2011; Woodhouse, 2017). In forests, double-bounce scattering can also occur between tree trunks and the ground, particularly in flooded vegetation, making it useful for wetland monitoring (Freeman & Durden, 1998; Richards, 2009). Polarimetric SAR is especially effective at detecting this mechanism, since double-bounce often manifests as strong co-polarized (HH, VV) signals, allowing separation from surface and volume scattering through decomposition methods (Yamaguchi et al., 2005).

In co-polarized channels, double-bounce from orthogonal dihedrals (e.g., building-ground) can dominate HH under many urban and flooded-forest conditions, while rough surface scattering often yields strong VV at moderate incidence angles; cross-polarized HV/VH responses increase with volume scattering from randomly oriented elements such as foliage. Relative magnitudes depend on wavelength, polarization, incidence angle, and surface moisture, and are best interpreted through polarimetric decomposition (Freeman & Durden, 1998; Richards, 2022; Van Zyl & Kim, 2011; Woodhouse, 2017; Yamaguchi et al., 2005).



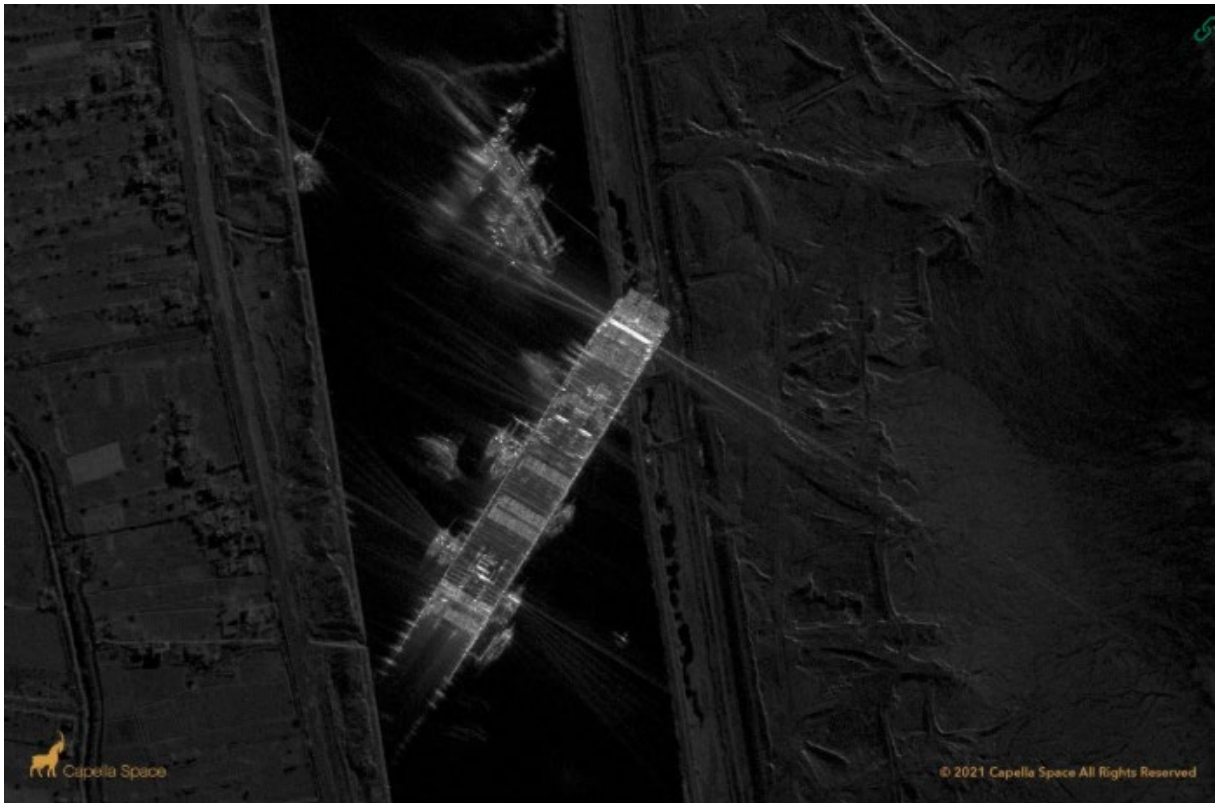


Figure 31: Ever Given container ship blocks the Suez Canal (Source: Capella Space (2021, <https://www.capellaspace.com/gallery/ever-given-container-ship-blocks-the-suez-canal/>) showing Double Bounce Effects at the back of the ship.

#### 4.4. Advanced SAR Techniques: InSAR

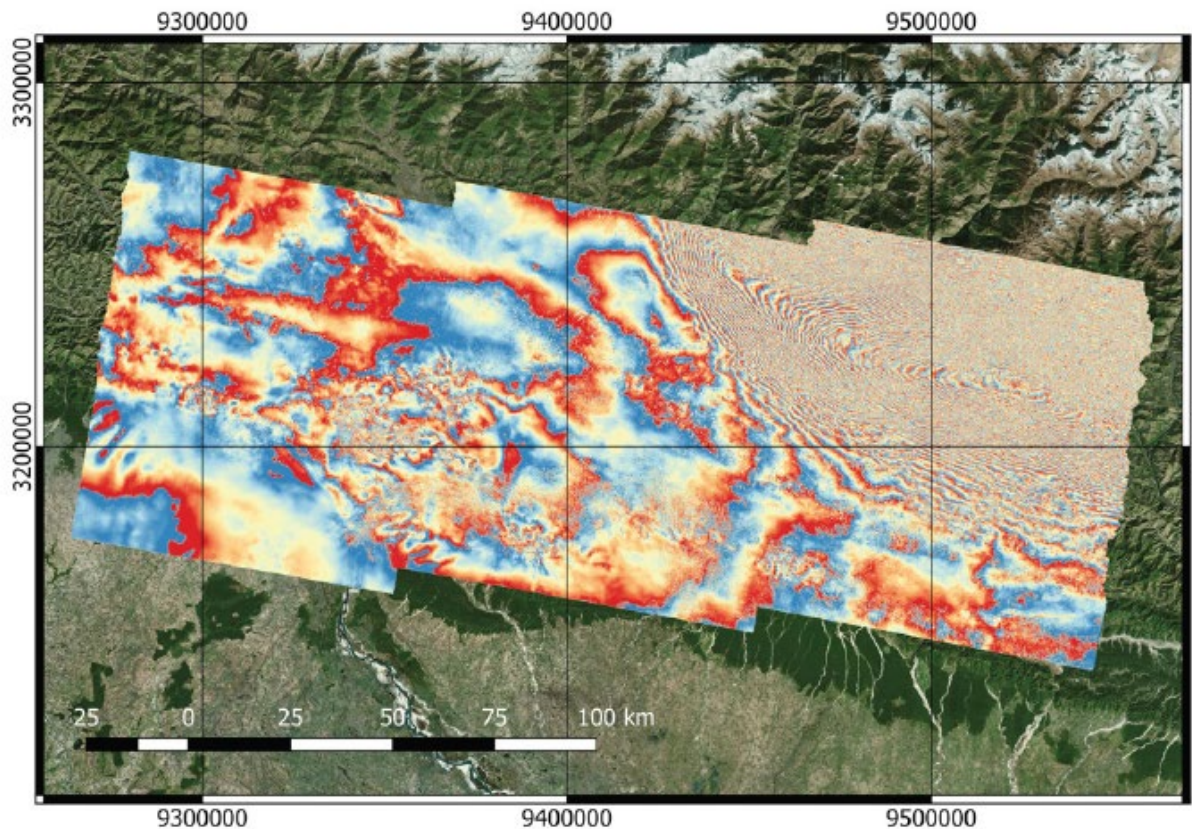


Figure 1: Geocoded Gorkha earthquake interferogram mapped in QGIS. The interferogram is used measure and map ground deformation with very high precision (Flores et al., 2019).

One of the most powerful applications of SAR is interferometry (InSAR), which measures phase differences between two or more acquisitions of the same area to derive elevation models and ground deformation with centimeter-level precision. InSAR has been used to map earthquake displacements, monitor volcanic activity, and measure glacier velocities. Time series approaches such as Persistent Scatterer InSAR and Small Baseline Subset InSAR extend these methods to monitor deformation over years with millimetric precision, making them invaluable for urban infrastructure monitoring and hazard assessment (Bamler & Hartl, 1998; Ferretti et al., 2001; Flores et al., 2019).

Coherence analysis, which quantifies the correlation between successive SAR acquisitions, is a powerful tool for change detection. A reduction in coherence reflects physical modifications of the scattering surface, such as building collapse, flooding, or vegetation disturbance, and has been widely applied in disaster monitoring and land cover studies (Woodhouse, 2017). Polarimetric SAR, on the other hand, provides access to the scattering matrix and enables decomposition of backscattered signals into their physical components. Techniques such as the Freeman-Durden three-component model (Freeman & Durden, 1998) and the Yamaguchi four-component model (Yamaguchi et al., 2005) have been developed to separate surface, double-bounce, and volume scattering contributions, offering insights into vegetation structure, soil conditions, and urban environments. Together, coherence analysis and polarimetric decomposition demonstrate the versatility of SAR as an active sensing technique that extends well beyond the capabilities of optical systems (Van Zyl & Kim, 2011).



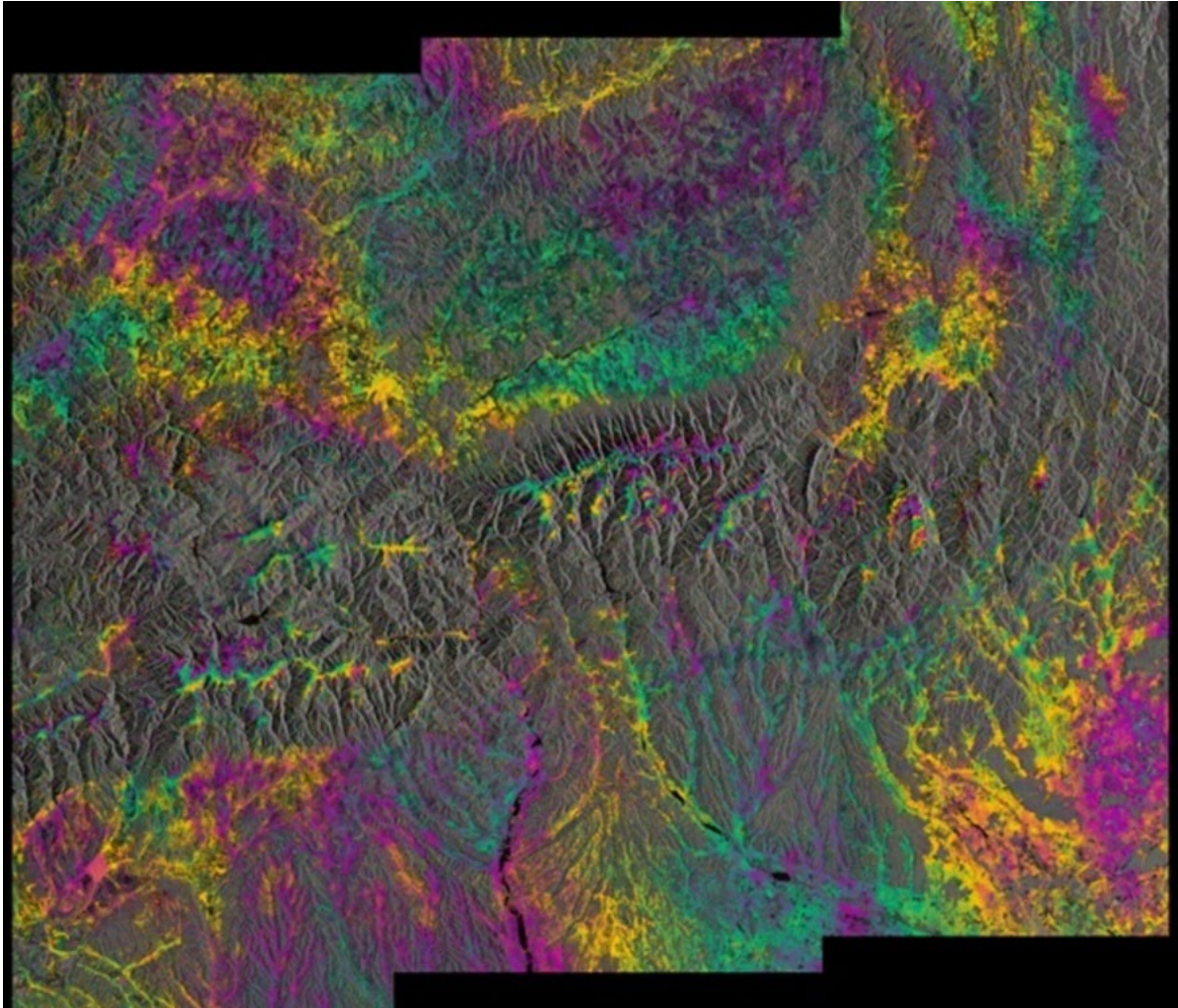


Figure 32: Sentinel 1: interferometric SAR (InSAR) Image. Source: ESA

## 5. Glossary and Definitions

### **Active Sensor**

A remote sensing system that generates its own energy, transmits it toward the Earth, and records the backscattered return. Examples include radar and lidar, which allow day-and-night, all-weather observations.

### **Atmospheric Correction**

The process of removing atmospheric effects (scattering, absorption) from remote sensing data to retrieve accurate surface reflectance values.

### **Backscatter**

The portion of an emitted radar signal that is scattered back toward the sensor. Its magnitude and polarization depend on the target's roughness, geometry, and dielectric properties.

### **Biomass Estimation**

Quantification of vegetation biomass using remote sensing, often relying on SAR backscatter sensitivity to canopy structure and density.

### **Coherence**

A measure of correlation between two or more SAR acquisitions. High coherence indicates stability of the scatterers, while loss of coherence reveals changes such as vegetation growth, building collapse, or flooding.

### **Electromagnetic Spectrum**

The full range of electromagnetic radiation, from gamma rays to radio waves. Remote sensing typically uses visible, infrared, and microwave regions.

### **Foreshortening / Layover / Shadow**

Geometric distortions specific to SAR imaging geometry. Foreshortening compresses slopes, layover causes tall objects to appear displaced toward the sensor, and shadow occurs where terrain blocks illumination.

### **Hyperspectral Remote Sensing**

Imaging technology that records hundreds of narrow, contiguous spectral bands, enabling the detection of diagnostic absorption features for vegetation, minerals, or water quality.

### **Interferometric SAR (InSAR)**

A radar technique that exploits phase differences between two or more SAR images of the same scene to measure surface topography and ground deformation with centimeter to millimeter accuracy.

### **Landsat Program**

A joint NASA-USGS mission series launched in 1972 that provides the longest continuous record of optical Earth observation.



## **Multispectral Remote Sensing**

Collection of reflected radiation in several discrete spectral bands, enabling classification of land cover and vegetation indices. Sentinel-2 and Landsat are prime examples.

### **Normalized Difference Water Index (NDWI - McFeeters, 1996)**

A spectral index using green and near-infrared (NIR) reflectance to enhance the detection and delineation of open water features in multispectral imagery. The green NIR formulation increases contrast between water bodies and terrestrial surfaces, making it widely applied for hydrological mapping and flood monitoring.

### **Normalized Difference Water Index (NDWI also called NDII - Gao, 1996)**

A spectral index using near-infrared (NIR) and shortwave infrared (SWIR) reflectance to estimate vegetation liquid water content. The NIR-SWIR formulation reduces soil and atmospheric background effects while being sensitive to changes in leaf and canopy water status, supporting drought monitoring and vegetation stress analysis.

## **Passive Sensor**

A sensor that relies on naturally available energy (typically solar radiation or Earth's thermal emission). Examples: Landsat OLI, Sentinel-2 MSI, MODIS.

## **Polarization (SAR)**

The orientation of the electric field vector of a radar wave. SAR systems commonly use horizontal (H) or vertical (V) transmit/receive channels, leading to four combinations: HH, HV, VH, VV. Each channel emphasizes different scattering mechanisms (surface, double-bounce, or volume).

## **Radar Cross Section (RCS)**

A measure of the strength of a target's radar return, expressed in square meters. Influenced by size, shape, roughness, dielectric constant, and incidence angle.

## **Scattering Mechanisms**

Processes by which radar signals interact with targets. Includes:

- **Specular scattering** (smooth surfaces, low return)
- **Diffuse scattering** (rough surfaces, strong return)
- **Volume scattering** (multiple scattering within vegetation or snow, often cross-polarized)
- **Double-bounce scattering** (efficient reflection between vertical and horizontal surfaces, typical of urban areas).

## **Speckle**

Granular noise in SAR images caused by coherent interference of scattered signals within a resolution cell. It reduces interpretability but contains statistical information.

## **Synthetic Aperture Radar (SAR)**

An active microwave imaging system that synthesizes a long antenna by combining Doppler-shifted echoes along a flight path, achieving high spatial resolution independent of weather or daylight.

## Vegetation Indices

Mathematical combinations of spectral bands designed to highlight vegetation properties, such as NDVI, NDWI (water index), NBR (burn index), and MSAVI (soil-adjusted index).

## 6. Acronyms and Abbreviations

Acronym	Full Term	Description / Context
<b>AOI</b>	Area of Interest	Geographic region selected for analysis in remote sensing or GIS workflows.
<b>AVIRIS</b>	Airborne Visible/Infrared Imaging Spectrometer	NASA airborne hyperspectral sensor (400-2500 nm).
<b>BOA</b>	Bottom of Atmosphere	Corrected reflectance at surface level after atmospheric effects are removed.
<b>CASI</b>	Compact Airborne Spectrographic Imager	Airborne hyperspectral imager for environmental monitoring.
<b>CHIME</b>	Copernicus Hyperspectral Imaging Mission for the Environment	Upcoming ESA hyperspectral mission.
<b>DEM</b>	Digital Elevation Model	Raster dataset representing ground elevation.
<b>DSM</b>	Digital Surface Model	Raster dataset including ground + structures (buildings, vegetation).
<b>ESA</b>	European Space Agency	Operator of Sentinel and EnMAP missions.
<b>ETM+</b>	Enhanced Thematic Mapper Plus	Landsat 7 multispectral sensor.
<b>FLAASH</b>	Fast Line-of-sight Atmospheric Analysis of Spectral Hypercubes	Atmospheric correction tool for hyperspectral imagery.
<b>HH, HV, VH, VV</b>	Polarization Channels	Linear SAR polarizations: H = horizontal, V = vertical; co- and cross-pol combinations.
<b>InSAR</b>	Interferometric Synthetic Aperture Radar	SAR technique using phase differences for topography/deformation mapping.
<b>IW</b>	Interferometric Wide Swath	Sentinel-1 acquisition mode with ~250 km swath.
<b>JERS</b>	Japanese Earth Resources Satellite	L-band SAR mission (JAXA, 1992-1998).
<b>LCLUC</b>	Land Cover / Land Use Change	Remote sensing theme analyzing land transitions.
<b>MODIS</b>	Moderate Resolution Imaging Spectroradiometer	NASA multispectral instrument on Terra/Aqua.
<b>MSAVI</b>	Modified Soil Adjusted Vegetation Index	Vegetation index correcting soil reflectance effects.
<b>MSI</b>	MultiSpectral Instrument	Sentinel-2 optical sensor (13 bands).

<b>NBR</b>	Normalized Burn Ratio	Index using SWIR/NIR for fire severity mapping.
<b>NDVI</b>	Normalized Difference Water Index	spectral index using green and near-infrared (NIR) reflectance to enhance the detection and delineation of open water features
<b>NDVI (NDII)</b>	Normalized Difference Vegetation Index	Vegetation greenness index (NIR vs. Red).
<b>NDWI</b>	Normalized Difference Water Index	Water body detection index (Green vs. NIR).
<b>NIR</b>	Near Infrared	Spectral region (~0.7-1.3 $\mu\text{m}$ ).
<b>NISAR</b>	NASA-ISRO Synthetic Aperture Radar	Forthcoming L- and S-band SAR mission.
<b>NOAA</b>	National Oceanic and Atmospheric Administration	U.S. operator of meteorological satellites.
<b>OLI</b>	Operational Land Imager	Landsat 8/9 multispectral sensor.
<b>PALSAR</b>	Phased Array type L-band Synthetic Aperture Radar	SAR sensor onboard ALOS/ALOS-2.
<b>PolInSAR</b>	Polarimetric Interferometric SAR	Technique combining polarimetry and interferometry to retrieve vegetation structure.
<b>PoISAR</b>	Polarimetric SAR	Quad-polarization SAR imaging (HH, HV, VH, VV).
<b>PRI</b>	Photochemical Reflectance Index	Index sensitive to photosynthetic efficiency.
<b>PRISMA</b>	PRecursor IperSpettrale della Missione Applicativa	Italian spaceborne hyperspectral mission (2019-).
<b>RCMRD</b>	Regional Centre for Mapping of Resources for Development	ESA/SERVIR partner institution in Kenya.
<b>RCS</b>	Radar Cross Section	Quantitative measure of radar backscatter strength.
<b>REDD+</b>	Reducing Emissions from Deforestation and Forest Degradation	International forest carbon monitoring framework (appears in doc).
<b>RS</b>	Remote Sensing	Acquisition of Earth observation data from spaceborne, airborne, or UAV platforms.
<b>SAR</b>	Synthetic Aperture Radar	Active microwave imaging technique.
<b>SBAS</b>	Small Baseline Subset InSAR	Multi-temporal InSAR method for deformation monitoring.
<b>SBG</b>	Surface Biology and Geology	Planned NASA hyperspectral mission.
<b>SLAR</b>	Side-Looking Airborne Radar	Early airborne radar imaging system.
<b>SLC</b>	Single Look Complex	SAR data format containing amplitude + phase.
<b>SWIR</b>	Shortwave Infrared	Spectral region (~1.3-2.5 $\mu\text{m}$ ).
<b>TOPSAR</b>	Terrain Observation with Progressive Scans SAR	Sentinel-1 wide-swath imaging mode.
<b>UAV</b>	Unmanned Aerial Vehicle	Drone platforms used in remote sensing.
<b>VNIR</b>	Visible and Near Infrared	Spectral region covering visible to ~1.0 $\mu\text{m}$ .
<b>EO</b>	Earth Observation	General term for monitoring the Earth with satellites and sensors.

## 7. List of Figures

Figure 1: Sentinel-2 Satellite, Source: ESA .....	1
Figure 2: Theory of remote sensing of the earth Electromagnetic spectrum of energy radiations Remote sensing platforms with Sensors on board (Omuto et al., 2012) .....	3
Figure 3: DJI Matrice 300 RTK Drone equipped with Zenmuse P1 camera during the mission at Fuglebekken catchment. (Alphonse et al., 2023).....	4
Figure 4: Graphical Abstract (Alphonse et al., 2023) .....	4
Figure 5: From the real world to an image of it, to scene reconstruction. Image from UNIGIS Salzburg based on (Blaschke, 2010).....	5
Figure 6: Active and Passive Sensors. Source: NASA.....	6
Figure 7: The electromagnetic spectrum typically used in remote sensing, and spectral reflectance curves show the distinct signatures of vegetation, soil, and water, which are fundamental for interpretation (Jensen, 2016). .....	7
Figure 8: Monochrome, multispectral and hyperspectral imaging visualized (Mehta et al., 2018) .....	8
Figure 9: Sentinel 2 - Optical Image / True Colour Composite. Source: ESA .....	9
Figure 10: False colour composite with RGB and NIR, Source: ESA Sentinel-2 .....	10
Figure 11: the electromagnetic spectrum and the transmittance through earth's atmosphere (Richards, 2022).....	12
Figure 12: Indicative transmission spectra of the seven most significant atmospheric constituents, the water vapour curve is for a tropical atmosphere (Richards, 2022) .....	13
Figure 13: Variations of spectral indices calculation to measure specific features of the spectra (Viviano et al., 2014).....	14
Figure 14: Principle of SAM: An unclassified point in feature space (x) will be assigned to that class to which it has the smallest spectral angle (here: b) (Spectral Angle Mapper Processor - ESA, n.d.) .....	15
Figure 15: Principle of linear mixtures (Bioucas-Dias et al., 2012).....	16
Figure 16: Complete pathway from raw data to results, using spectral unmixing (Bioucas-Dias et al., 2012) .....	17
Figure 17: Radar of the type used for detection of aircraft. It rotates steadily, sweeping the airspace with a narrow beam. Air Force Museum, Hatzerim, Israel. Source: Wikipedia .....	19
Figure 18: Side Looking Radar: Resolution of targets spatially by time resolution of the received echoes. (Richards, 2009) .....	20
Figure 19: Echoes received back by the Antenna (European Space Agency, 2007) .....	21
Figure 20: Imaging geometry for a side-looking radar system (Van Zyl & Kim, 2011).....	21
Figure 21: Conceptual sketch of the dependence of surface roughness on the sensor wavelength $\lambda$ : (a) smooth, (b) intermediate, and (c) rough. (Flores et al., 2019) .....	23
Figure 22: Main geometric distortions on SAR images with their dependence on acquisition geometry: (a) foreshortening, (b) layover, and (c) shadow. (Flores et al., 2019).....	24
Figure 23: Penetration of different wavelengths for different materials (Meyer, 2019) .....	25
Figure 24: : Polarization of sent and received waves (based on images from ESA) (European Space Agency, 2007).....	26
Figure 25: Illustration of how different polarizations (HH, VV, HV, and color composites) bring out different features in an agricultural scene from California's Central Valley. The different orchards and crops in this area display different polarized backscatter behavior (Flores et al., 2019, p. 219) .....	27



Figure 26: Illustration of the speckle effect from Singh et al. (2021). (a) Agricultural fields showing a grainy texture caused by (c) constructive and (d) destructive interference of backscattered waves (b).....	28
Figure 27: Radar backscattering mechanisms for different SAR wavelengths: X- and C-band (left) and L-band (right) (Ottinger & Kuenzer, 2020) .....	29
Figure 28: Backscatter: Total effect of the backscatter values in urban detection (Liao & Wen, 2020) .....	30
Figure 29: Illustration of main scattering types for SAR data (Meyer, 2019) .....	31
Figure 30: Double Bounce (Flores et al., 2019, p. 28) .....	32
Figure 31: Ever Given container ship blocks the Suez Canal (Source: Capella Space (2021, <a href="https://www.capellaspace.com/gallery/ever-given-container-ship-blocks-the-suez-canal/">https://www.capellaspace.com/gallery/ever-given-container-ship-blocks-the-suez-canal/</a> ) showing Double Bounce Effects at the back of the ship. ....	33
Figure 32: Sentinel 1: interferometric SAR (InSAR) Image. Source: ESA .....	35

## 8. List of Tables

Table 1: Overview of Hyperspectral Sensors. Specifications compiled from : (Babey & Anger, 1993; Barnsley et al., 2004; Cocks et al., 1998; Green et al., 1998; Headwall Photonics - Hyperspectral Imaging Systems & Components, n.d.; Table 1 Spectral Characteristics of the CASI Data, n.d.; Kirrilly Pfitzner, 2004; Loizzo et al., 2018; Miko, n.d.; S. Murchie et al., 2007; S. L. Murchie et al., 2009; Pearlman et al., 2003; van der Meer et al., 2012). For UAV-based platforms: Spatial resolution is a typical GSD range for low-altitude UAV operations with standard optics, and that true instrument specifications are spectral range, number of bands, and spectral sampling (Headwall Photonics - Hyperspectral Imaging Systems & Components, n.d.) .....	11
Table 2: SAR Bands (Flores et al., 2019) as well as internet research on K-band.....	23
Table 3: Possible polarisation modes (European Space Agency, 2007) .....	26

## 9. References

1. Adams, J. B., Smith, M. O., & Johnson, P. E. (1986). Spectral mixture modeling: A new analysis of rock and soil types at the Viking Lander 1 Site. *Journal of Geophysical Research: Solid Earth*, 91(B8), 8098–8112. <https://doi.org/10.1029/JB091iB08p08098>
2. Alphonse, A. B., Wawrzyniak, T., Osuch, M., & Hanselmann, N. (2023). Applying UAV-Based Remote Sensing Observation Products in High Arctic Catchments in SW Spitsbergen. *Remote Sensing*, 15(4), 934. <https://doi.org/10.3390/rs15040934>
3. Babey, S. K., & Anger, C. D. (1993). Compact airborne spectrographic imager (CASI): a progress review. *Imaging Spectrometry of the Terrestrial Environment, 1937*, 152–163. <https://doi.org/10.1117/12.157052>
4. Bamler, R., & Hartl, P. (1998). Synthetic aperture radar interferometry. *Inverse Problems*, 14(4), R1. <https://doi.org/10.1088/0266-5611/14/4/001>
5. Barnsley, M. J., Settle, J. J., Cutter, M. A., Lobb, D. R., & Teston, F. (2004). The PROBA/CHRIS mission: a low-cost smallsat for hyperspectral multiangle observations of the Earth surface and atmosphere. *IEEE Transactions on Geoscience and Remote Sensing*, 42(7), 1512–1520. <https://doi.org/10.1109/TGRS.2004.827260>
6. Berger, M., Moreno, J., Johannessen, J. A., Levelt, P. F., & Hanssen, R. F. (2012). ESA's sentinel missions in support of Earth system science. *Remote Sensing of Environment*, 120, 84–90. <https://doi.org/10.1016/j.rse.2011.07.023>
7. Bioucas-Dias, J. M., Plaza, A., Dobigeon, N., Parente, M., Du, Q., Gader, P., & Chanussot, J. (2012). Hyperspectral Unmixing Overview: Geometrical, Statistical, and Sparse Regression-Based Approaches. *IEEE Journal of Selected Topics in Applied Earth Observations and Remote Sensing*, 5(2), 354–379. <https://doi.org/10.1109/JSTARS.2012.2194696>
8. Blaschke, T. (2010). Object based image analysis for remote sensing. *ISPRS Journal of Photogrammetry and Remote Sensing*, 65(1), 2–16. <https://doi.org/10.1016/j.isprsjprs.2009.06.004>
9. Boardman, J. W. (1993, October 25). *Automating spectral unmixing of AVIRIS data using convex geometry concepts*. <https://ntrs.nasa.gov/citations/19950017428>

10. Clark, R. N., Swayze, G. A., Livo, K. E., Kokaly, R. F., Sutley, S. J., Dalton, J. B., McDougal, R. R., & Gent, C. A. (2003). Imaging spectroscopy: Earth and planetary remote sensing with the USGS Tetracorder and expert systems. *Journal of Geophysical Research: Planets*, 108(E12). <https://doi.org/10.1029/2002JE001847>
11. Cocks, T., Jenssen, R., Stewart, A., Wilson, I., & Shields, T. (1998). The hymaptm airborne hyperspectral sensor: The system, calibration and performance. *1st EARSEL Workshop on Imaging Spectroscopy*.
12. Cumming, I. G., & Wong, F. H. (2005). Digital processing of synthetic aperture radar data. *Artech House*, 1(3), 108–110.
13. Deledalle, C.-A., Denis, L., & Tupin, F. (2009). Iterative Weighted Maximum Likelihood Denoising With Probabilistic Patch-Based Weights. *IEEE Transactions on Image Processing*, 18(12), 2661–2672. <https://doi.org/10.1109/TIP.2009.2029593>
14. Delegido, J., Verrelst, J., Alonso, L., & Moreno, J. (2011). Evaluation of Sentinel-2 Red-Edge Bands for Empirical Estimation of Green LAI and Chlorophyll Content. *Sensors*, 11(7), 7063–7081. <https://doi.org/10.3390/s110707063>
15. Drusch, M., Del Bello, U., Carlier, S., Colin, O., Fernandez, V., Gascon, F., Hoersch, B., Isola, C., Laberinti, P., Martimort, P., Meygret, A., Spoto, F., Sy, O., Marchese, F., & Bargellini, P. (2012). Sentinel-2: ESA's Optical High-Resolution Mission for GMES Operational Services. *Remote Sensing of Environment*, 120, 25–36. <https://doi.org/10.1016/j.rse.2011.11.026>
16. European Space Agency. (2007). *ASAR product handbook* [Manual]. ESA. <https://earth.esa.int/eogateway/documents/20142/37627/ASAR-Product-Handbook.pdf>
17. Ferretti, A., Prati, C., & Rocca, F. (2001). Permanent scatterers in SAR interferometry. *IEEE Transactions on Geoscience and Remote Sensing*, 39(1), 8–20. <https://doi.org/10.1109/36.898661>
18. Flores, A., Herndon, K., Thapa, R., & Cherrington, E. (2019). *Synthetic Aperture Radar (SAR) Handbook: Comprehensive Methodologies for Forest Monitoring and Biomass Estimation*. <https://doi.org/10.25966/NR2C-S697>

19. Freeman, A., & Durden, S. L. (1998). A three-component scattering model for polarimetric SAR data. *IEEE Transactions on Geoscience and Remote Sensing*, 36(3), 963–973. <https://doi.org/10.1109/36.673687>
20. Frost, V. S., Stiles, J. A., Shanmugan, K. S., & Holtzman, J. C. (1982). A Model for Radar Images and Its Application to Adaptive Digital Filtering of Multiplicative Noise. *IEEE Transactions on Pattern Analysis and Machine Intelligence*, PAMI-4(2), 157–166. <https://doi.org/10.1109/TPAMI.1982.4767223>
21. Gamon, J. A., Peñuelas, J., & Field, C. B. (1992). A narrow-waveband spectral index that tracks diurnal changes in photosynthetic efficiency. *Remote Sensing of Environment*, 41(1), 35–44. [https://doi.org/10.1016/0034-4257\(92\)90059-S](https://doi.org/10.1016/0034-4257(92)90059-S)
22. Gao, B.-C. (1996). NDWI—A normalized difference water index for remote sensing of vegetation liquid water from space. *Remote Sensing of Environment*, 58(3), 257–266.
23. Goetz, A. F., Vane, G., Solomon, J. E., & Rock, B. N. (1985). Imaging spectrometry for Earth remote sensing. *Science (New York, N.Y.)*, 228(4704), 1147–1153. <https://doi.org/10.1126/science.228.4704.1147>
24. Green, R. O., Eastwood, M. L., Sarture, C. M., Chrien, T. G., Aronsson, M., Chippendale, B. J., Faust, J. A., Pavri, B. E., Chovit, C. J., Solis, M., Olah, M. R., & Williams, O. (1998). Imaging Spectroscopy and the Airborne Visible/Infrared Imaging Spectrometer (AVIRIS). *Remote Sensing of Environment*, 65(3), 227–248. [https://doi.org/10.1016/S0034-4257\(98\)00064-9](https://doi.org/10.1016/S0034-4257(98)00064-9)
25. Guanter, L., Kaufmann, H., Segl, K., Foerster, S., Rogass, C., Chabrillat, S., Kuester, T., Hollstein, A., Rossner, G., Chlebek, C., Straif, C., Fischer, S., Schrader, S., Storch, T., Heiden, U., Mueller, A., Bachmann, M., Mühle, H., Müller, R., ... Sang, B. (2015). The EnMAP Spaceborne Imaging Spectroscopy Mission for Earth Observation. *Remote Sensing*, 7(7), 8830–8857. <https://doi.org/10.3390/rs70708830>
26. *Headwall Photonics - Hyperspectral Imaging Systems & Components*. (n.d.). Headwall Photonics. <https://headwallphotonics.com/>
27. Heinz, D. C. & Chein-I-Chang. (2001). Fully constrained least squares linear spectral mixture analysis method for material quantification in hyperspectral imagery. *IEEE Transactions on Geoscience and Remote Sensing*, 39(3), 529–545. <https://doi.org/10.1109/36.911111>



28. James B. Campbell & Randolph H. Wynne. (2011). *Introduction to Remote Sensing* (5th ed., Vol. 5). Guilford Press, New York. <https://www.mdpi.com/2072-4292/5/1/282>
29. Jensen, J. R. (2016). *Introductory digital image processing: a remote sensing perspective* (4th ed). Pearson Education.
30. Justice, C. O., Vermote, E., Townshend, J. R. G., Defries, R., Roy, D. P., Hall, D. K., Salomonson, V. V., Privette, J. L., Riggs, G., Strahler, A., Lucht, W., Myneni, R. B., Knyazikhin, Y., Running, S. W., Nemani, R. R., Wan, Z., Huete, A. R., van Leeuwen, W., Wolfe, R. E., ... Barnsley, M. J. (1998). The Moderate Resolution Imaging Spectroradiometer (MODIS): land remote sensing for global change research. *IEEE Transactions on Geoscience and Remote Sensing*, 36(4), 1228–1249. <https://doi.org/10.1109/36.701075>
31. Key, C. H., & Benson, N. C. (2006). Landscape assessment (LA). In: Lutes, Duncan C.; Keane, Robert E.; Caratti, John F.; Key, Carl H.; Benson, Nathan C.; Sutherland, Steve; Gangi, Larry J. 2006. *FIREMON: Fire Effects Monitoring and Inventory System. Gen. Tech. Rep. RMRS-GTR-164-CD. Fort Collins, CO: US Department of Agriculture, Forest Service, Rocky Mountain Research Station. p. LA-1-55, 164.*
32. Kirrilly Pfitzner. (2004). Compact Airborne Spectrographic Imager (CASI) and ground-based spectrometer data of Nabarlek - an overview. *ResearchGate*. [https://www.researchgate.net/publication/314230990\\_Compact\\_Airborne\\_Spectrographic\\_Imager\\_CASI\\_and\\_ground-based\\_spectrometer\\_data\\_of\\_Nabarlek\\_-\\_an\\_overview](https://www.researchgate.net/publication/314230990_Compact_Airborne_Spectrographic_Imager_CASI_and_ground-based_spectrometer_data_of_Nabarlek_-_an_overview)
33. Kruse, F. A., Lefkoff, A. B., Boardman, J. W., Heidebrecht, K. B., Shapiro, A. T., Barloon, P. J., & Goetz, A. F. H. (1993). The spectral image processing system (SIPS)—interactive visualization and analysis of imaging spectrometer data. *Remote Sensing of Environment*, 44(2), 145–163. [https://doi.org/10.1016/0034-4257\(93\)90013-N](https://doi.org/10.1016/0034-4257(93)90013-N)
34. Lee, J. S., Grunes, M. R., Ainsworth, T. L., Schuler, D. L., & Cloude, S. R. (n.d.). *Coherence Estimation and Speckle Filtering Based on Scattering Properties. 2*, 705–707. <https://doi.org/10.1109/igarss.2003.1293890>
35. Lee, J.-S. (1980). Digital image enhancement and noise filtering by use of local statistics. *IEEE Transactions on Pattern Analysis and Machine Intelligence*, PAMI-2(2), 165–168. <https://doi.org/10.1109/TPAMI.1980.4766994>

36. Liao, H.-Y., & Wen, T.-H. (2020). Extracting urban water bodies from high-resolution radar images: Measuring the urban surface morphology to control for radar's double-bounce effect. *International Journal of Applied Earth Observation and Geoinformation*, 85, 102003. <https://doi.org/10.1016/j.jag.2019.102003>
37. Loizzo, R., Guarini, R., Longo, F., Scopa, T., Formaro, R., Facchinetti, C., & Varacalli, G. (2018). Prisma: The Italian Hyperspectral Mission. *IGARSS 2018 - 2018 IEEE International Geoscience and Remote Sensing Symposium*, 175–178. <https://doi.org/10.1109/IGARSS.2018.8518512>
38. McFEETERS, S. K. (1996). The use of the Normalized Difference Water Index (NDWI) in the delineation of open water features. *International Journal of Remote Sensing*, 17(7), 1425–1432. <https://doi.org/10.1080/01431169608948714>
39. Mehta, N., Shaik, S., Devireddy, R., & Gartia, M. R. (2018). Single-Cell Analysis Using Hyperspectral Imaging Modalities. *Journal of Biomechanical Engineering*, 140(2), 020802. <https://doi.org/10.1115/1.4038638>
40. Meyer, F. (2019). Spaceborne Synthetic Aperture Radar: Principles, data access, and basic processing techniques. *Synthetic Aperture Radar (SAR) Handbook: Comprehensive Methodologies for Forest Monitoring and Biomass Estimation*, 21–64.
41. Miko. (n.d.). Aisa Systems. *Specim*. <https://www.specim.com/aisa/>
42. Moreira, A., Prats-Iraola, P., Younis, M., Krieger, G., Hajnsek, I., & Papathanassiou, K. P. (2013). A tutorial on synthetic aperture radar. *IEEE Geoscience and Remote Sensing Magazine*, 1(1), 6–43. <https://doi.org/10.1109/MGRS.2013.2248301>
43. Murchie, S., Arvidson, R., Bedini, P., Beisser, K., Bibring, J.-P., Bishop, J., Boldt, J., Cavender, P., Choo, T., Clancy, R. T., Darlington, E. H., Des Marais, D., Espiritu, R., Fort, D., Green, R., Guinness, E., Hayes, J., Hash, C., Heffernan, K., ... Wolff, M. (2007). Compact Reconnaissance Imaging Spectrometer for Mars (CRISM) on Mars Reconnaissance Orbiter (MRO). *Journal of Geophysical Research: Planets*, 112(E5). <https://doi.org/10.1029/2006JE002682>
44. Murchie, S. L., Seelos, F. P., Hash, C. D., Humm, D. C., Malaret, E., McGovern, J. A., Choo, T. H., Seelos, K. D., Buczkowski, D. L., Morgan, M. F., Barnouin-Jha, O. S., Nair, H., Taylor, H. W., Patterson, G. W., Harvel, C. A., Mustard, J. F., Arvidson, R. E., McGuire, P., Smith, M. D., ...

- Poulet, F. (2009). Compact Reconnaissance Imaging Spectrometer for Mars investigation and data set from the Mars Reconnaissance Orbiter's primary science phase. *Journal of Geophysical Research: Planets*, 114(E2). <https://doi.org/10.1029/2009JE003344>
45. Omuto, C., Nachtergaele, F., & Vargas, R. (2012). *State of the Art Report on Global and Regional Soil Information: Where are we? Where to go?*
46. Ottinger, M., & Kuenzer, C. (2020). Spaceborne L-band synthetic aperture radar data for geoscientific analyses in coastal land applications: a review. *Remote Sensing*, 12(14), Article 2228. <https://doi.org/10.3390/rs12142228>
47. Pearlman, J. S., Barry, P. S., Segal, C. C., Shepanski, J., Beiso, D., & Carman, S. L. (2003). Hyperion, a space-based imaging spectrometer. *IEEE Transactions on Geoscience and Remote Sensing*, 41(6), 1160–1173. <https://doi.org/10.1109/TGRS.2003.815018>
48. Plaza, A., Martín, G., Plaza, J., Zortea, M., & Sánchez, S. (2011). Recent Developments in Endmember Extraction and Spectral Unmixing. In S. Prasad, L. M. Bruce, & J. Chanussot (Eds.), *Optical Remote Sensing: Advances in Signal Processing and Exploitation Techniques* (pp. 235–267). Springer. [https://doi.org/10.1007/978-3-642-14212-3\\_12](https://doi.org/10.1007/978-3-642-14212-3_12)
49. Qi, J., Chehbouni, A., Huete, A. R., Kerr, Y. H., & Sorooshian, S. (1994). A modified soil adjusted vegetation index. *Remote Sensing of Environment*, 48(2), 119–126. [https://doi.org/10.1016/0034-4257\(94\)90134-1](https://doi.org/10.1016/0034-4257(94)90134-1)
50. Richards, J. A. (2009). *Remote Sensing with Imaging Radar*. Springer. <https://doi.org/10.1007/978-3-642-02020-9>
51. Richards, J. A. (2022). *Remote Sensing Digital Image Analysis*. Springer International Publishing. <https://doi.org/10.1007/978-3-030-82327-6>
52. Small, D. (2011). Flattening Gamma: Radiometric Terrain Correction for SAR Imagery. *IEEE Transactions on Geoscience and Remote Sensing*, 49(8), 3081–3093. <https://doi.org/10.1109/TGRS.2011.2120616>
53. *Spectral Angle Mapper Processor* - ESA. (n.d.). <https://step.esa.int/main/wp-content/help/versions/9.0.0/snap-toolboxes/org.esa.s2tbx.s2tbx.spectral.angle.mapper.ui/sam/SAMProcessor.html>

54. *Table 1 Spectral Characteristics of the CASI data.* (n.d.). ResearchGate. [https://www.researchgate.net/figure/Spectral-Characteristics-of-the-CASI-data\\_tbl1\\_314230990](https://www.researchgate.net/figure/Spectral-Characteristics-of-the-CASI-data_tbl1_314230990)
55. Thenkabail, P. S., & Lyon, J. G. (Eds.). (2016). *Hyperspectral Remote Sensing of Vegetation*. CRC Press. <https://doi.org/10.1201/b11222>
56. Thenkabail, P. S., Lyon, J. G., & Huete, A. (2011). *Hyperspectral remote sensing of vegetation*. <https://doi.org/10.1201/b11222>
57. Torres, R., Snoeij, P., Geudtner, D., Bibby, D., Davidson, M., Attema, E., Potin, P., Rommen, B., Floury, N., Brown, M., Traver, I. N., Deghaye, P., Duesmann, B., Rosich, B., Miranda, N., Bruno, C., L'Abbate, M., Croci, R., Pietropaolo, A., ... Rostan, F. (2012). GMES Sentinel-1 mission. *Remote Sensing of Environment*, 120, 9–24. <https://doi.org/10.1016/j.rse.2011.05.028>
58. Tucker, C. J. (1979). Red and photographic infrared linear combinations for monitoring vegetation. *Remote Sensing of Environment*, 8(2), 127–150.
59. Ulaby, F. T., Moore, R. K., & Fung, A. K. (1981). *Microwave Remote Sensing: Active and Passive, Vol. 1* (Vol. 1). Artech House.
60. van der Meer, F. D., van der Werff, H. M. A., van Ruitenbeek, F. J. A., Hecker, C. A., Bakker, W. H., Noomen, M. F., van der Meijde, M., Carranza, E. J. M., Smeth, J. B. de, & Woldai, T. (2012). Multi- and hyperspectral geologic remote sensing: A review. *International Journal of Applied Earth Observation and Geoinformation*, 14(1), 112–128. <https://doi.org/10.1016/j.jag.2011.08.002>
61. Van Zyl, J., & Kim, Y. (2011). *Synthetic aperture radar polarimetry*. Wiley. <https://doi.org/10.1002/9781118116104>
62. Viviano, C. E., Seelos, F. P., Murchie, S. L., Kahn, E. G., Seelos, K. D., Taylor, H. W., Taylor, K., Ehlmann, B. L., Wiseman, S. M., Mustard, J. F., & Morgan, M. F. (2014). Revised CRISM spectral parameters and summary products based on the currently detected mineral diversity on Mars. *Journal of Geophysical Research: Planets*, 119(6), 1403–1431. <https://doi.org/10.1002/2014JE004627>

63. Watson-Watt, R. (1946). The evolution of radiolocation. *Journal of the Institution of Electrical Engineers-Part I: General*, 93(69), 374–382.
64. Woodhouse, I. H. (2017). *Introduction to Microwave Remote Sensing*. CRC Press. <https://doi.org/10.1201/9781315272573>
65. Wulder, M. A., Loveland, T. R., Roy, D. P., Crawford, C. J., Masek, J. G., Woodcock, C. E., Allen, R. G., Anderson, M. C., Belward, A. S., Cohen, W. B., Dwyer, J., Erb, A., Gao, F., Griffiths, P., Helder, D., Hermosilla, T., Hipple, J. D., Hostert, P., Hughes, M. J., ... Zhu, Z. (2019). Current status of Landsat program, science, and applications. *Remote Sensing of Environment*, 225, 127–147. <https://doi.org/10.1016/j.rse.2019.02.015>
66. Yamaguchi, Y., Moriyama, T., Ishido, M., & Yamada, H. (2005). Four-component scattering model for polarimetric SAR image decomposition. *IEEE Transactions on Geoscience and Remote Sensing*, 43(8), 1699–1706. <https://doi.org/10.1109/TGRS.2005.852084>



## 10. Disclaimer

The preparation of this thesis involved a structured workflow combining extensive manual reading, systematic literature management, and selective use of AI-based tools to support efficiency and consistency. The primary foundation of the work rests on the author's direct engagement with the scientific literature, critical assessment of sources, and manual drafting of summaries and arguments. Artificial intelligence was employed as an auxiliary tool, never as a replacement for scholarly judgment.

Approximately 165 scientific papers relevant to the topic of battlefield damage assessment of urban structures were initially identified via Google Scholar searches. These publications were imported into Zotero, where each entry was supplemented with a full-text PDF and an associated structured note. Notes followed a standardized template including metadata, extracted data fields (keywords, models, datasets, satellites, methods), and a layered summary (context, methodology, results, conclusions). Each referenced paper was read and evaluated by the author; summaries were drafted manually, supported where appropriate by Adobe AI-generated abstracts, which were always verified and corrected against the original texts.

Markdown notes were processed through a custom Python pipeline that normalized metadata, extracted datasets and satellites, created keywords, and ensured interoperability with Obsidian for relational graph visualization. AI support was used here primarily Regex in the Python pipeline. For technical tasks such as metadata normalization, DOI resolution, and error checking of bibliographic entries Python scripts were used. For the identification of highly cited primary works, ChatGPT 4.0/5 (Version of July / August 2025) was employed in conjunction with relational graph analyses; candidate references were cross-verified manually via Google Scholar citation counts before inclusion.

Draft chapters of the appendices and literature overview were written manually, based on the structured notes and critical reading. ChatGPT was subsequently used in an editorial capacity to propose rephrasings, ensure consistency in academic style, and generate alternative formulations. The AI-generated text was not adopted verbatim; instead, it was carefully fact-checked, compared with the cited sources, and revised by the author. Similarly, scite.ai was used as a supplementary tool to verify the context of citations within the scientific discourse. All final references were inserted manually via Zotero to ensure accuracy and compliance with citation standards.

This integrated workflow allowed for efficient processing of a large body of literature while ensuring academic integrity. The critical reading, interpretation, selection of relevant findings, structuring of arguments, and final phrasing of all content were conducted by the author. AI tools contributed to metadata processing, drafting of preliminary summaries, language refinement, and bibliometric checks, but the responsibility for accuracy, interpretation, and argumentation rests fully with the author.